DOI: 10.1002/aic.17438

PERSPECTIVE

AIChE JOURNAL

Engineering of inorganic nanostructures with hierarchy of chiral geometries at multiple scales

Anastasia Visheratina | Prashant Kumar | Nicholas Kotov

Biointerfaces Institute, University of Michigan, Ann Arbor, Michigan, USA

Correspondence
Nicholas Kotov, Biointerfaces Institute, University of Michigan, Ann Arbor, MI.
Email: kotov@umich.edu

Funding information
Office of Naval Research Multidisciplinary University Research Initiative Award, Grant/Award Number: ONR N00014-18-1-2497; NSF project "Energy- and Cost-Efficient Manufacturing Employing Nanoparticles", Grant/Award Numbers: DMR-9871177, 1538180, 1566460, 1463474; Vannevar Bush DoD Fellowship, Grant/Award Number: ONR N000141812876

1 | CHIRALITY AND CHEMICAL ENGINEERING

A chiral object is one that is non-superimposable on its mirror image by rotational and translational operations. Chirality has unifying fundamental importance for physics, chemistry, astronomy, mathematics, biology, and medicine.[1,2] It is important to emphasize that the discovery of chirality and subsequent proliferation of the concepts of mirror asymmetry in these sciences were prompted by chemical engineering research. Chirality of chemical compounds was discovered by Louis Pasteur (Figure 1), who at that time was investigating the causes of wine spoilage. Pasteur's studies were commissioned by the chemical engineering practitioners —wine and spirit makers of France.[3] At age 25, Pasteur discovered the optical implications of chirality in 1848 while analyzing sodium ammonium tartrate crystals under a microscope.[4] He observed two types of crystals that were similar but not identical because these crystals were non-superimposable mirror images of each other. A few years later, Pasteur made a conclusion, which became the foundation of stereochemistry: chirality of molecules leads to chirality of their crystals. Solutions of these compounds are optically active, that is, they rotate the plane of linearly polarized light in opposite directions.[4] Subsequently, in 1874, van't Hoff[5] and Le Bel[6] independently proposed that molecular asymmetry could result from the tetrahedral arrangement (configuration) of four different groups on an atom. The formal definition of chirality was given by Lord Kelvin in the Baltimore Lectures on Molecular Dynamics and the Wave Theory of Light in 1904: "*I call any geometrical figure, or group of points, chiral, and say that it has chirality if its image in a plane mirror, ideally realized, cannot be brought to coincide with itself*".[7] Note that this definition was given many years later after the actual discovery of the role and some practical implications of chirality in chemical processes.

Since these times molecules with non-superimposable mirror images are referred to as enantiomers. Among many possible mirror-asymmetrical geometries, chemical technologies are associated with two of them more often than others—tetrahedrons and helices. When an sp^3 carbon with tetrahedral geometry has four different substituents, it is chiral and is typically referred to as an optical center, a stereocenter, or a chiral carbon. Simple molecules with one optical center, such as proteinogenic amino acids (AAs), are designated as *L*- or *D*-enantiomers according to the Fischer-Rosanoff convention established in 1906.[8] Sugars and AAs with the same relative configuration as (+)-glyceraldehyde are assigned *D* (from the Latin *dexter*, meaning "right"), and the same as (−)-glyceraldehyde are assigned *L* (from the Latin *laevus*, meaning "left").

Because only relative polarization rotation data and chemical configuration of optical centers could be determined at the beginning of the 20th century, limited information was available about the relationship between optical polarization rotation and the chemical structure of the compound giving rise to the rotation. *L*- or *D*-notations cannot be used to determine the absolute geometric configuration or the rotation of polarized light, and, thus, a list of chirality descriptors for chemical structures was eventually expanded to include optical properties and other chiral geometries. While *D*- and *L*- notations correspond

On occasion of his 2020 Alpha Chi Sigma Award for Chemical Engineering Research AIChE.

FIGURE 1 Louis Pasteur in laboratory of University of Strasbourg studying fermentation. Reproduced from https://www.britannica.com/biography/Louis-Pasteur

to the spatial arrangement of atoms around the chirality center (or molecule configuration), the prefixes (+) or (−) used above refers to the actual optical activity of the substance: whether it rotates the plane of polarized light clockwise (+) or counterclockwise (−). In 1951, Bijvoet et al.[9] established the absolute configuration (the exact spatial arrangement of atoms independent of other molecules) of sodium rubidium (+)-tartrate tetrahydrate using X-ray crystallographic methods. This finding was reconfirmed in 2008 by Lutz and Schreurs using modern XRD techniques combined with the computational processing of the scattering data.[10] In 1956, Cahn, Ingold, and Prelog proposed a convention[11] (i.e., Cahn-Ingold-Prelog rule) that allowed the designation of the absolute configuration at chiral centers in organic molecules in three-dimensional space. According to a specific set of rules based on atomic numbers, the absolute configuration is designated either as *R* (from the Latin *rectus*, meaning "right, in the sense of being correct") or *S* (from the Latin *sinister*, meaning "left, improper"). Note that *R/S* designations cannot be used to predict the direction of polarization rotation.

Axial chirality is a standard geometry of mirror-asymmetric molecules exemplified by allenes and substituted biphenyls.[12] These molecules do not have a chiral center but an axis of chirality, about which a set of substituents is held in a spatial arrangement that is not superposable on its mirror image. The enantiomers of axially chiral compounds are usually designated as R_a and S_a, where the asymmetric element is referred to as an improper axis. Molecules may have an improper axis of symmetry but not being chiral, with the best example being the tetrahedral CH_4 molecule.

Helices represent another standard chiral geometry encountered in biomolecules, biological assemblies, tissues, and organs.[13] In organic chemistry, helices are widely presented by helicenes and their derivatives,[14] in inorganic chemistry—by multiple inorganic nano- and micro-structures.[15,16] Helices rotating in a counterclockwise manner are typically referred to as left-handed or **Λ**-enantiomers, whereas those rotating clockwise are referred to as right-handed or **Δ**-enantiomers. All of these geometries are unified by the possession of a screw axis of symmetry, a typical element of chiral structures at the macro scale.

2 | VARIETY OF SCALES FOR CHIRAL INORGANIC NANOSTRUCTURES

Several extensive reviews on chiral inorganic nanoparticles (NPs) and their assemblies were published over the last few years that described, in various degrees of detail, the chiral nanostructures known today.[17–30] Along with their preparation and optical properties, these works also discuss their potential applications which include but not limited to chiral catalysis, enantiospecific separation, biosensing, chiral memory, and chiroptical devices. The most important properties of chiral nanostructures upbearing their applications are (1) strong absorption of circularly polarized light (CPL) and (2) enantioselective interactions with biological objects. For brevity, we will not repeat the common points between these reviews but rather focus on the foundational concepts (Section 2), optical properties (Section 3), and chemical methods (Section 4) being used for *engineering* their structures and properties. To accomplish this, we must first describe the nature of chirality in inorganic nanostructures and their properties. There are distinct similarities and vast differences in the ways chirality manifests in nanostructures compared to traditional chemical compounds and biomolecules.

2.1 | Molecular-scale chirality

Mirror asymmetry in NPs and their assemblies is nearly always present at multiple scales and with numerous geometrical elements, making the traditional notations used in organic and inorganic chemistry (*R*, *S*) only partially applicable. Except for a few notable cases where the chirality of the nanoscale structures is imparted by illumination with circularly polarized photons,[31–34] the primary contribution to the chirality of nanostructures is associated with *organic molecules that are chemically bound to their surface*. These organic molecules, or surface ligands, represent molecular scale asymmetry embedded in NP structures and are directly relevant to the engineering of all nano- and microstructures. Mirror asymmetries at the same scale can also arise from the binding of achiral molecules to the NPs, creating an optical center that is topologically similar to those in *L*- and *D*-AAs.[35]

The secondary contribution to chirality is related to the NPs *organic–inorganic interface* that engenders new hybrid electronic states formed between the organic molecules on the surface and the NPs inorganic core. The molecular orbitals describing these electronic states can be strongly asymmetric, which gives rise to the quantum level of chirality. The existence of such orbitals was first established for CdSe NPs,[36]

revealing the hybridization between the highest occupied molecular orbitals of surface atoms with those of the chiral ligand. This phenomenon was subsequently found in other nanomaterials as well.[37–39]

2.2 | Nanometer-scale chirality

As the physical dimensions of chiral geometries are increased, the third contributor to the chirality of nanostructures arises from the surface itself. The difference between the previous case of interfacial states and the surface chirality is that the former one refers to the quantum electronic states formed between organic groups and the inorganic phase, while the latter one refers to the geometry of the surface overall, that is in nanoscale for most cases. The surface distribution of stabilizing ligands is non-random and can be mirror-asymmetric, which becomes especially obvious for small nanoscale clusters.[40] It is worth mentioning that individual surface facets of even bulk symmetric solids can be chiral and many complex metal oxides can also exhibit low-energy chiral surfaces.[41,42]

The scale of chiral geometries transitions to nanoscale in at least two (curved) dimensions while remaining at the molecular scale in the third. In this sense, surface chirality can be treated as semi-dimensional because it is dominated by planar asymmetry. Applying methods of non-Euclidean space geometry allows for the description of the mirror asymmetry of the NPs in curved space.

The next level of chirality, also associated with nanometer-scale geometries, is the crystal lattice of the NPs. Atomic packing in the inorganic phase during the formation of NP cores is affected by the chirality of the surface ligands, which can be particularly strong for small NPs (e.g., 2–3 nm).[43,44] The evidence of chiral distortions of the inorganic lattice of NPs was also observed experimentally for CdS NPs stabilized with

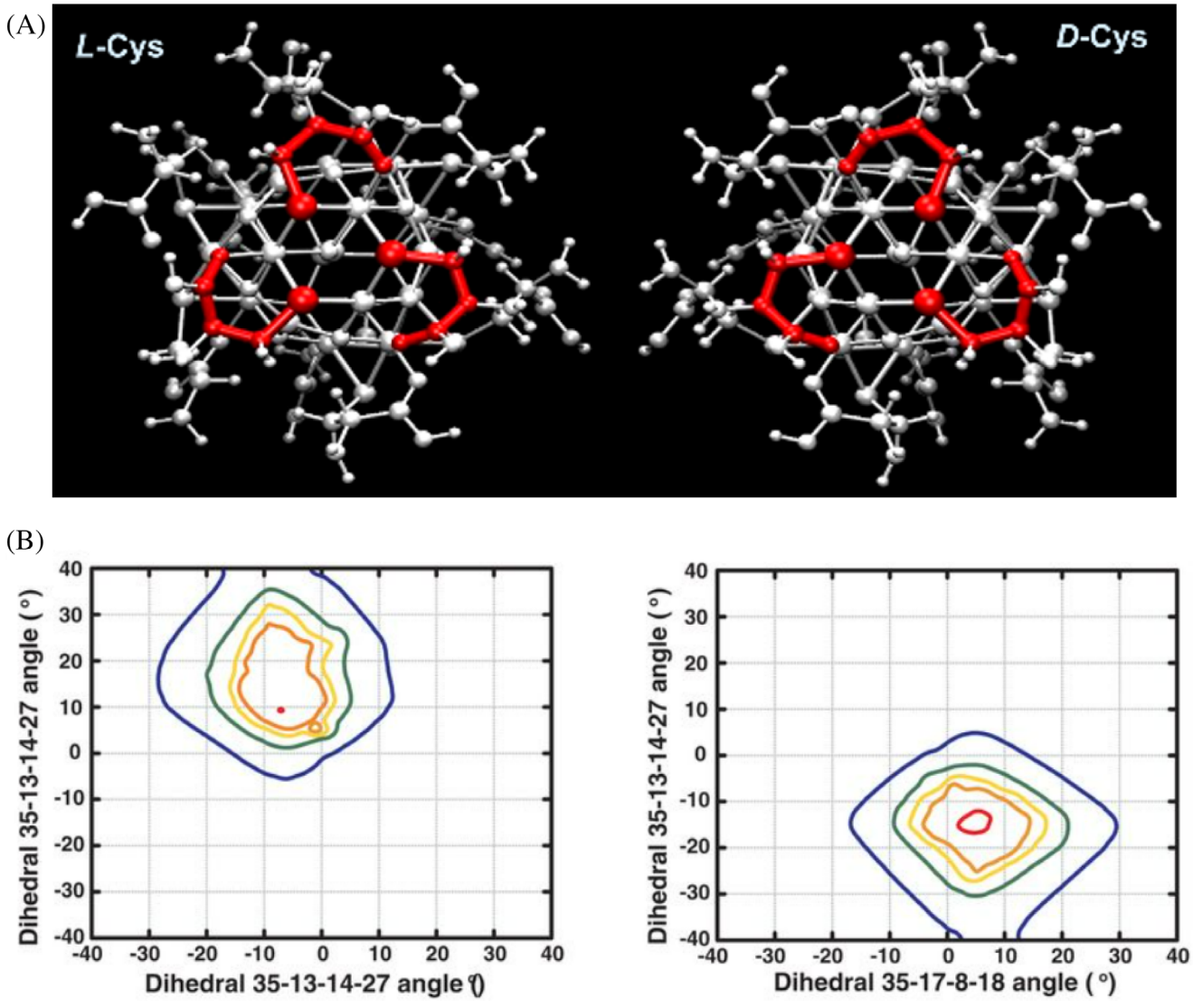

FIGURE 2 (A) *L*-Cys and *D*-Cys Co_3O_4 NPs; (B) Ramachadran plots for chiral Co_3O_4 NPs functionalized with either M-D-Cys (left) or P-L-Cys (right). Three ligands on each corner of the tetrahedral model NP formed ring-like structures with either a clockwise (M) or a counterclockwise (P) sense of rotation with respect to the C_3 axis. Adapted with permission from Ref. 43 Copyright © 2018 The Authors, some rights reserved; exclusive licensee American Association for the Advancement of Science

penicillamine (Pen),[45] cysteine methyl ester hydrochloride-stabilized CdTe NPs,[46] and Co_3O_4 NPs stabilized with cysteine (Cys).[43] The chiral distortions of the atomic lattice in small NPs can also be observed computationally (Figure 2A), for example, in Co_3O_4 and WO_{3-x} NPs.[43,47] The Ramachandran plots, used extensively in structural biology, can be applied to visualize and analyze such distortions (Figure 2B).

All of these contributions to mirror asymmetries have characteristic dimensions of these chiral elements, that is, ~1–3 nm. As the NPs become larger, the distortions of the crystal lattice caused by surface ligands disappear for the core, but they may be retained in certain situations.

Mirror asymmetry of the surface ligands can also preferentially bias the chiral defects in the inorganic core, which can be exemplified by screw and edge dislocations for various semiconductor NPs (Figure 3A), nanowires, dendrites, carbon nanotubes, and Au nanoplates.[48,50–54] Recent studies revealed that screw dislocations mediate chirality transfer between crystal structure and morphology of model tellurium nanocrystals, and geometrical chirality is not an outcome of the chiral crystal structure or ligands.[55]

The next level of nanoscale chirality is related to the overall geometry of the NPs that is sometimes referred to as intrinsic or geometrical chirality. Small NPs with zinc-blende crystal lattices were shown to have truncated tetrahedral shapes,[31,35,56,57] which is geometrically homologous to an sp^3 carbon in optical centers.[35] Consequently, mirror-asymmetric tetrahedrons emerge at the nanometer scale when all four corners of the NP tetrahedron are different. For example, the small CdTe NPs can have truncated tetrahedral shapes and have been observed using transmission electron microscopy (TEM, Figure 3B). Considering that non-spherical NPs are commonly found in Nature, the chirality of NPs is not surprising. When the shapes are random, the particle dispersions are racemic.[32] The presence of the chiral bias ether due to AAs, circularly polarized photons, or intrinsically chiral crystal lattices changes the NP growth patterns and shifts the distribution of the NP shapes during synthesis toward one or the other chiral geometry.[32,58] For example, this effect can be seen for complex chiral shapes with propeller-like geometries because of the preferred growth on high index planes.[59]

2.3 | Meso- and micro-scale chirality

Mirror-asymmetry of chiral molecules and individual NPs can be transferred into the chirality of their assemblies, which represents the next scale and contribution to chirality in nanostructures. In the simplest case, it leads to mirror-asymmetric superstructures from nanoscale components with the characteristic scale of chirality in between ~20 nm[32,60–63] and ~10 μm.[64–66] For example, the observation of twisted nanosheets with a 1300 nm pitch is a clear demonstration how mirror asymmetry at the nanometer and micrometer length scales emerges due to the chirality transfer from molecular components of nanostructures.[64] The chirality transfer in NP assemblies can be governed by hydrogen bonding, entropic, and dispersive interactions. The interactions at NP-NP interfaces may result in enantiopure chiral helices[67,68] or twisted ribbons.[31]

A large class of chiral assemblies of NPs can also be created via templating by biomolecules that could be treated as external source of chirality.[17] In this case, the NP building blocks may be racemic or nearly achiral (spheres, rods, triangular nanoplates), and mirror asymmetry emerges during their preferential organization due to geometrically specific interactions with, for example, segments of DNA, proteins, peptides, lipids, sugars, etc. The chiral shapes of these structures can be nanorod pairs,[69–71] that can also develop into helical "log-stacks"[72] as more nanorods are added. Other geometrical shapes include left-handed (**Λ**) and right-handed (**Δ**) helices obtained by folding DNA strands.[73] Complex chiral shapes can also be obtained by interconnecting NPs with multiple "springs" represented by DNA.[74] Their chirality may not be initially obvious by visual comparison with familiar mirror-asymmetric shapes, such as helices, but they can be identified using chirality measures, for instance, Osipov-Pickup-Dunmur index that changes sign depending on the handedness of the structure.[75]

Continuing the consideration of scale, one can foresee the translation of the chirality of NPs into sub-millimeter, millimeter, and macroscale.[76]

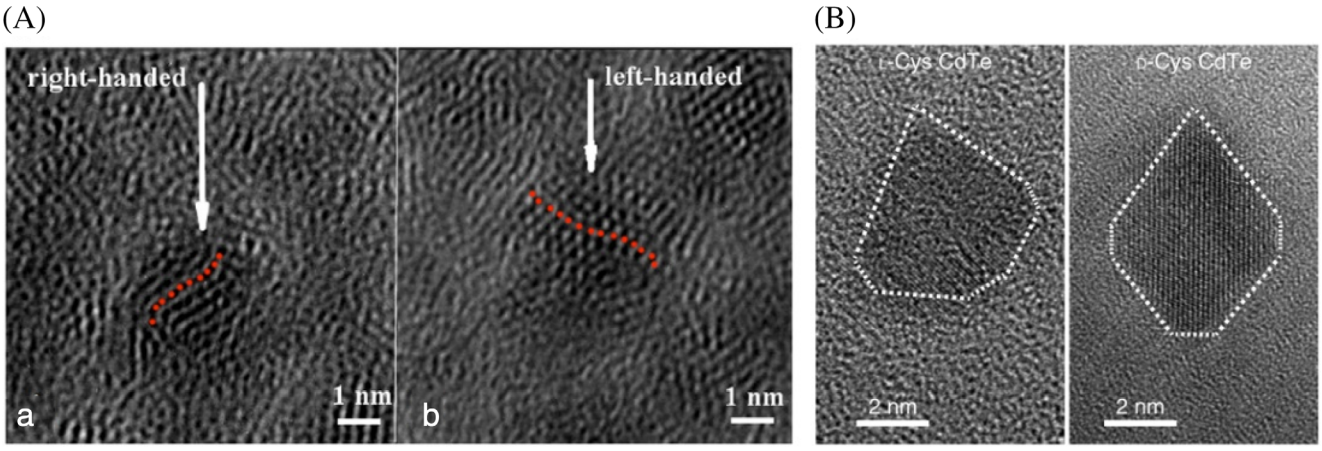

FIGURE 3 (A) TEM images of CdSe/ZnS NPs. The arrows indicate possible screw dislocations. Adapted with permission from Ref. 48 Copyright © 2015, American Chemical Society; (B) High-resolution TEM images of truncated tetrahedron-shaped (white dashed areas) *L*-Cys and *D*-Cys stabilized CdTe NPs. Adapted with permission from Ref. 49 Copyright © 2018, The Author(s)

2.4 | Connection with biology

Considering the rapid expansion of chiral nanostructures toward biology and medicine, it is instructive and insightful to draw parallels between hierarchical chirality in biological compounds and inorganic nanostructures. As a result of hydrogen bonds and other intermolecular interactions, AAs molecular scale chirality is transferred to the nanoscale chirality of proteins. Proteins are organized into four levels,[77] with chiral motifs at different scales (Figure 4A). The further self-assembly and aggregation of proteins can result in complex chiral structures at larger scales, for example, helical protein fibrils.[79] These phenomena demonstrate the distinct correlation between biological compounds and chiral inorganic NPs—hierarchical chirality (Figure 4B).

However, there are many differences, too, that researchers are in the process of understanding. One of them is the transfer of handedness of building blocks to the higher-order structures. While bioorganic molecules have the apparent stereochemical bias at the secondary structure level (Figure 4A), where right-handed helices are strongly preferred over left-handed helices, the usage of *L*-Cys as a chiral bias in the self-assembly of chiral inorganic nanostructures can result in both right-handed[67,80] and left-handed[67] helical structures. These finding clearly indicate that there is no deterministic transfer of handedness from one scale to another and having molecular components with, say, left symmetry does not mean by any measure that the nanoscale assembly must be also left. To some degree, this is also true in biology because our left and right hands are made from the same L-enantiomers of amino acids. Tracing the bifurcation point and the forces that control is important for both nanoscale inorganic and biological structures.

3 | OPTICAL PROPERTIES OF CHIRAL INORGANIC NANOSTRUCTURES

Chirality at multiple scales can be utilized as a metric for engineering NP and their assemblies. Before we discuss the practical approaches to engineering of chiral nanostructures, we need to discuss what the nanoscale design will be for and what are physical, chemical, and biological properties of the nanostructures that we aim to obtain. These properties are derivatives from the chiral geometry at multiple scales

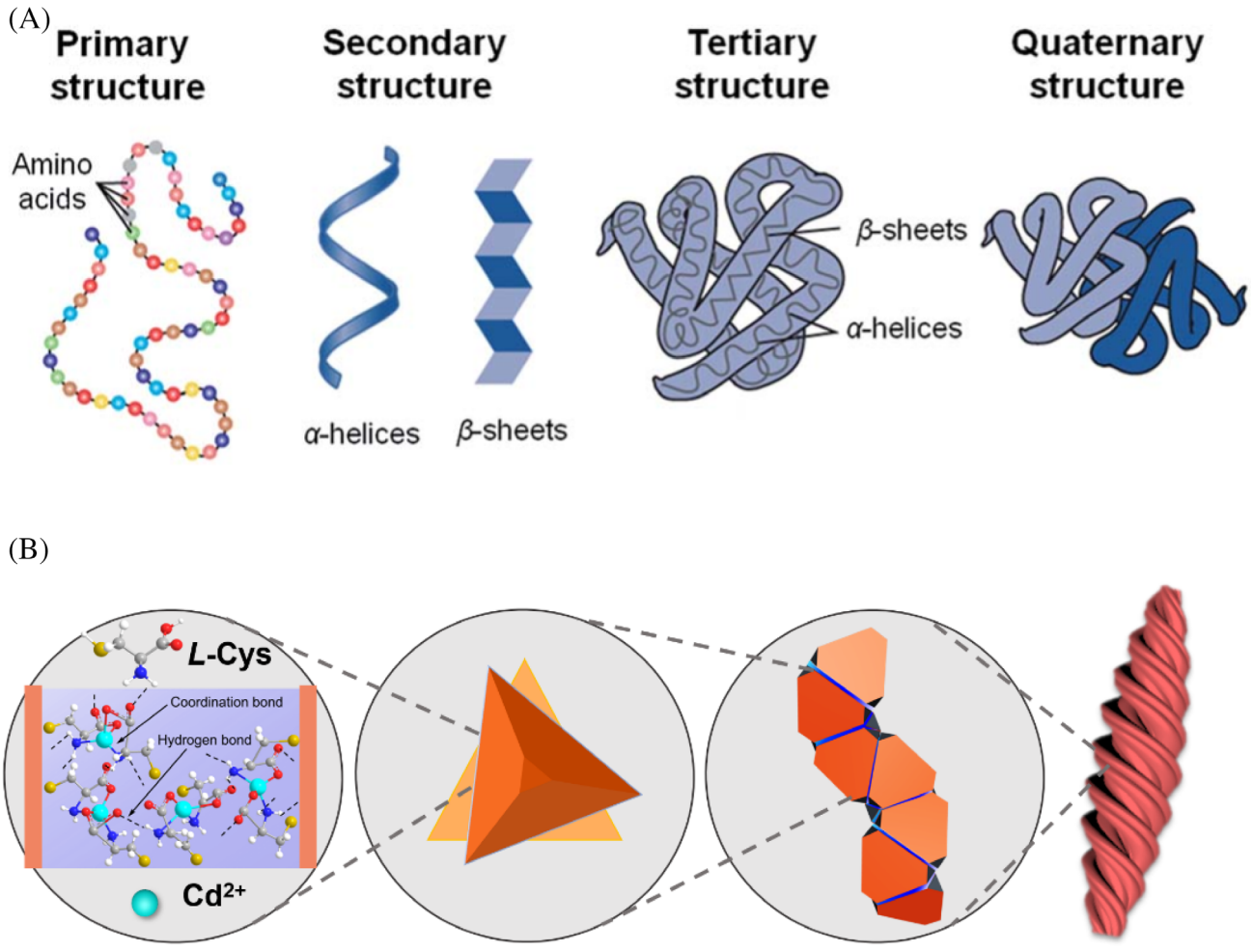

FIGURE 4 Hierarchical organization of (A) proteins and (B) self-assembled micron-scale Boerdijk–Coxeter–Bernal helices. Adapted with permission from Ref. 78 Copyright © 2013, Royal Society of Chemistry. Adapted with permission from Ref. 67 Copyright © 2020, American Chemical Society

and reflect the profound effects of chirality on optical, electrical, and magnetic effects specific to chiral materials. Chemical manifestations of chirality can be observed in catalysis, separations, and polymerization.[23] Chirality of NPs is also expected to have multiple implementations in biology that include their effect on drug delivery, cytotoxicity, cell signaling, cell adhesion.[81] All of these properties can be related to specific quantitative measures associated with chiral geometries exemplified by the Osipov-Pickup-Dunmur index calculated for the scale(s) characteristic for such properties. Note that additional measures of mirror asymmetry are likely to be needed in the future for establishing effective structure-property relationships this article, we will restrict the discussion to optical properties because they were investigated the best so far.

3.1 | Chirality and optical activity

The optical effects of chirality are typically observed by circular dichroism (CD) spectroscopy, which is based on differential absorption of left- and right-hand CPL by chiral compounds.[82] State-of-the-art CD spectrophotometers can measure across a wide spectral range, from far-ultraviolet (far-UV) to near-infrared (NIR). Other spectroscopic methods for measuring chirality include optical rotatory dispersion (ORD), Raman optical activity (ROA),[83] vibrational circular dichroism (VCD), and more recently, terahertz circular dichroism (TCD).[84] These methods cover various ranges of energies, linear and non-linear optical processes, and numerous reviews describe their technical details and various implementations.[85–89]

3.2 | Circular dichroism

CD spectra in the visible (Vis) or NIR range (intensity units are most often expressed in millidegrees) represent the ubiquitous tool to measure chiroptical activity of NP dispersions or thin films. For quantitative analysis of the chiroptical activity, the dissymmetry factor, or *g*-factor [$g = \Delta\varepsilon/\varepsilon = (\varepsilon_L - \varepsilon_R)/(\varepsilon_L + \varepsilon_R)$] is used, where $\Delta\varepsilon$ is the molar CD, ε is the molar extinction, and ε_L and ε_R are the molar extinction coefficients for left- and right-hand CPL, respectively. As a metric for materials design, g-factor reflects the strength of polarization rotation compared to the strength of light extinction, which is essential for multiple applications because it directly relates to the intensity of transmitted polarized light (rather than being dissipated) for a chiral material.

A valid CD experiment for comparing the chiroptical activity of two dispersions of enantiomers involves measuring the amplitudes of spectral bands with nearly equivalent extinction coefficients to avoid multiple concentration-depended processes such as agglomeration and scattering. For thin films, acquiring CD spectra requires even greater care to avoid artifacts from linear dichroism and circular birefringence. These measurements should be performed using Mueller matrix polarimetry[90] as it offers an unambiguous and mathematically robust platform for the analysis of light-matter interactions.[91]

Engineering chiroptical properties of materials includes maximization of CD amplitude and *g*-factor as well as 'tuning' of the chiroptical bands to specific wavelengths. Starting with the latter, the optical properties of nanostructures greatly expand the wavelength/frequency range of chiroptical activity compared to traditional chiral materials. While the typical range for the CD bands of AAs, proteins, and other biomolecules is in the UV region, organic dyes and metal coordination compounds can expand to the Vis and NIR ranges,[92–95] typically at the cost of chemical stability. The current palette of chiral inorganic nano- and microstructures includes materials with chiroptical activity in UV,[96] Vis,[97] NIR,[67] medium IR,[98] reaching as far as terahertz part of the electromagnetic spectrum.[84] Furthermore, the position of the bands and their simultaneous occurrence in different spectral windows can be fine-tuned by all the elements of chirality discussed in Section 2. Besides some nanomanufacturing techniques, resulting nanostructures can be economically produced by self-assembly using methods described in Section 4.

Inorganic chiral nanostructures have stronger chiroptical activity than that of similarly sized organic objects because of their high electrical polarizability and magnetic susceptibility.[17,99] While polarizabilities of some organic molecules can be ~2–100 Å^3, those of semiconductor NPs are ~10^4–10^5 Å^3, magnetic and metal NPs have polarizabilities of ~10^6 Å^3. The polarizabilities of NPs increase with their size,[99] which results in a marked increase of chiroptical activity in most cases. For example, increase of *g*-factors observed when transitioning from semiconductor NPs ($g = 10^{-5} - 10^{-4}$)[100] to semiconductor nanorods ($g = 10^{-4}$)[100] and semiconductor nanoplatelets ($g = 10^{-3}$).[101] This is particularly true for CD amplitudes based on the cumulative effects of light absorption and scattering.[31] However, this does not necessarily mean that with NP size increase, the CD strength of chiral NPs will increase. According to the Rosenfeld equation,[102] polarizability is only one of the multipliers that could affect the rotatory strength of matter. Therefore, decreasing other parameters while increasing NP size will not result in optical activity increase.[36,100]

An increase of optical asymmetry, that is, the ability of the material to rotate the polarization of light without dissipating it, is limited by scattering from nanostructures.[103] Most NPs and their assemblies are strong scatterers, leading to low *g*-factors. Theoretical works demonstrated that, due to the presence of a screw dislocation, nanocrystals of cylindrical shapes, such as semiconductor quantum disks, can have high *g*-factors up to 0.234,[104,105] which significantly exceed those of chiral molecules (~0.0001)[106] and are comparable with those of chiral plasmonic nanostructures (~0.3).[107]

Besides chiral crystal lattice distortions caused by mirror asymmetry of surface ligands and curved surface of nanostructures (see 2.2, Figure 2), Inorganic crystals can also have chiral crystal lattices. Non-centrosymmetric materials are not "exotic" with the hundreds of known non-centrosymmetric oxides.[108] Other bright examples are quartz, β-AgSe, α-HgS, selenium, tellurium. It is expected that NPs based on this arrangement should exhibit much stronger chiroptical activity compared to NPs with achiral space groups. Indeed, it was demonstrated that α-HgS NPs synthesized in the presence of chiral surface ligands, such as Pen, exhibited *g*-factors up to 0.012.[109] At the

same time, the chiroptical activities of CdS, CdSe, CdTe, and ZnS NPs with tethered chiral surface ligands were several orders of magnitude smaller, with *g*-factors less than 0.001.[109–111] The combination of chiral lattice and shape can increase the *g*-factors of nanomaterials even further.[112] An increase of *g*-factors can also be attained by increasing the long-range order in the NPs assemblies.[103]

At the quantum and molecular levels, the optical effects of chiral inorganic nanostructures observed by CD spectroscopy are weaker than those that arise from other chiral structural components. In other words, the contributions to CD from mirror asymmetries are more significant in scale and more substantial. For instance, individual CdTe NPs typically have weak chiroptical activity and low *g*-factor values on the order of 10^{-5}.[80] CdTe NPs assemble into mesoscale helices that exhibit *g*-factors up to ~0.01 at $\lambda = 900$ nm.[80]

3.3 | Circularly polarized light emission

The presence of chiral centers on the surface of NPs significantly contributes to their light-emitting properties and, in particular, the appearance of circularly polarized luminescence.[113] For example, *L*- and *D*-Cys ligands induced circularly polarized luminescence in the dispersions of CdSe NPs.[36] After emission, the polarization of the photons can be modified by the scattering from the NPs and other particles in the dispersion, as was observed for chiral complex structures.[64] In particular, at 650 nm, the polarization rotation of the emission from the quantum states in twisted Au-S nanosheets with *L*- or *D*-Cys surface ligands changed its sign but not the wavelength when the dispersed scatterers disassembled from micron-sized chiral complex structures to twisted nanosheets with ~1300 nm pitch. Therefore, along with mirror asymmetry of molecular orbitals giving rise to CPL emission from chiral nanostructures, one should also include practical and theoretical considerations on circularly polarized scattering that may also be referred to as differential scattering.[70,114]

4 | CHEMICAL PROCESSES USED IN ENGINEERING OF CHIRAL NANOSTRUCTURES

Based on the understanding of the multiscale chirality of inorganic nanostructures (Section 2) and the optical characteristics that one wants to attain (Section 3), let us now discuss how to create a wide range of chiral inorganic nanostructures. In this section, we will consider their engineering starting from quantum and molecular scale to nanometer and micrometer scale using established and emerging chemical engineering techniques. Examples of practical implementations for concrete chiral nanostructures will be provided for each method. Note that in many cases, and especially for the processes involving structures with chirality at nano-, meso-, and microscale, the chemical processes are intertwined, and the resulting structures are the products of chiral interactions at multiple scales occurring simultaneously. Among optical characteristics, we will pay special attention to the *g*-factor because it can be universally applied across different scales, concentration ranges, and has direct technological significance.

4.1 | Chirality transfer from surface ligands

Chiral NPs are commonly synthesized as dispersions in liquid media in the presence of chiral ligands, which serve as chiral bias. These ligands also act as stabilizers by imparting colloidal and thermodynamic stability to nanoscale colloids. Chirality transfer from chiral ligands to NPs occurs during the nucleation and arrested growth of NPs when chiral molecules attach to the NPs nucleating seeds and surface. Alternatively, this may take place when chiral molecules remain free in solution and generate the chiral environment around growing NPs.[115] Chirality of individual NPs can be further translated to complex structures and assemblies based on them. Despite the intensive studies in the field of chiral growth of NPs,[17] the correlation between the actual geometrical arrangements of atoms and corresponding optical activity of the resulting NPs is yet to be established.

The presence of chiral components during the crystallization process of relatively small NPs (~1–10 nm) leads to their asymmetric growth because various crystalline planes of achiral crystal lattices display different ligand density, ligand-NP bonds, and surface energy. The optical activity of these nanostructures can be tuned by careful adjustment of synthesis conditions, where both types of chiral molecules and their concentration were shown to be critical factors determining the growth of chiral nanocrystals.[67,116,117]

As demonstrated with NPs from tellurium,[112] structures with chiral lattice and achiral shape may be chiroptically silent for the spectral range associated with the electronic transitions of the core inorganic material. It directly depends on the quantum nature of electronic transitions associated with such crystal lattice and is a subject to the Brillouin zone selection rules. Te NPs of ~140 nm in length with both chiral lattice and shape have *g*-factors ~0.003. The significant contribution of the chiral shape rather than chiral lattice toward the chiroptical activity of NPs was supported by simulations of their optical properties. The type of chiral molecules used for the synthesis of tellurium nanostructures and their order of addition was found to affect the final shape of NPs. For instance, the addition of glutathione followed by hydrazine yielded long tellurium nanorods with small *g*-factors, while hydrazine and glutathione added in a reverse order resulted in tellurium nanocrystals, with higher *g*-factors.

Decoupling of chirality at atomic and nanometer scales in inorganic nanostructures can be achieved through epitaxial growth based on a two-step synthesis (Figure 5A)[58] starting with 12 nm α-HgS seeds. These NPs had well-defined crystallographic chirality due to the helical arrangement of Hg and S atoms along the *c* axis (Figure 5B). Slow, co-addition of Hg and S precursors ensured successive ion layer adsorption and reaction onto the seeds in excess of *D*- and *L*-Pen serving as chiral surface ligands. As a result, twisted triangular bipyramid nanostructures with chiral morphologies were obtained (Figure 5C). These structures had an average length and aspect ratio of 76.9 nm and 1.90, respectively. The optical properties of these nanostructures

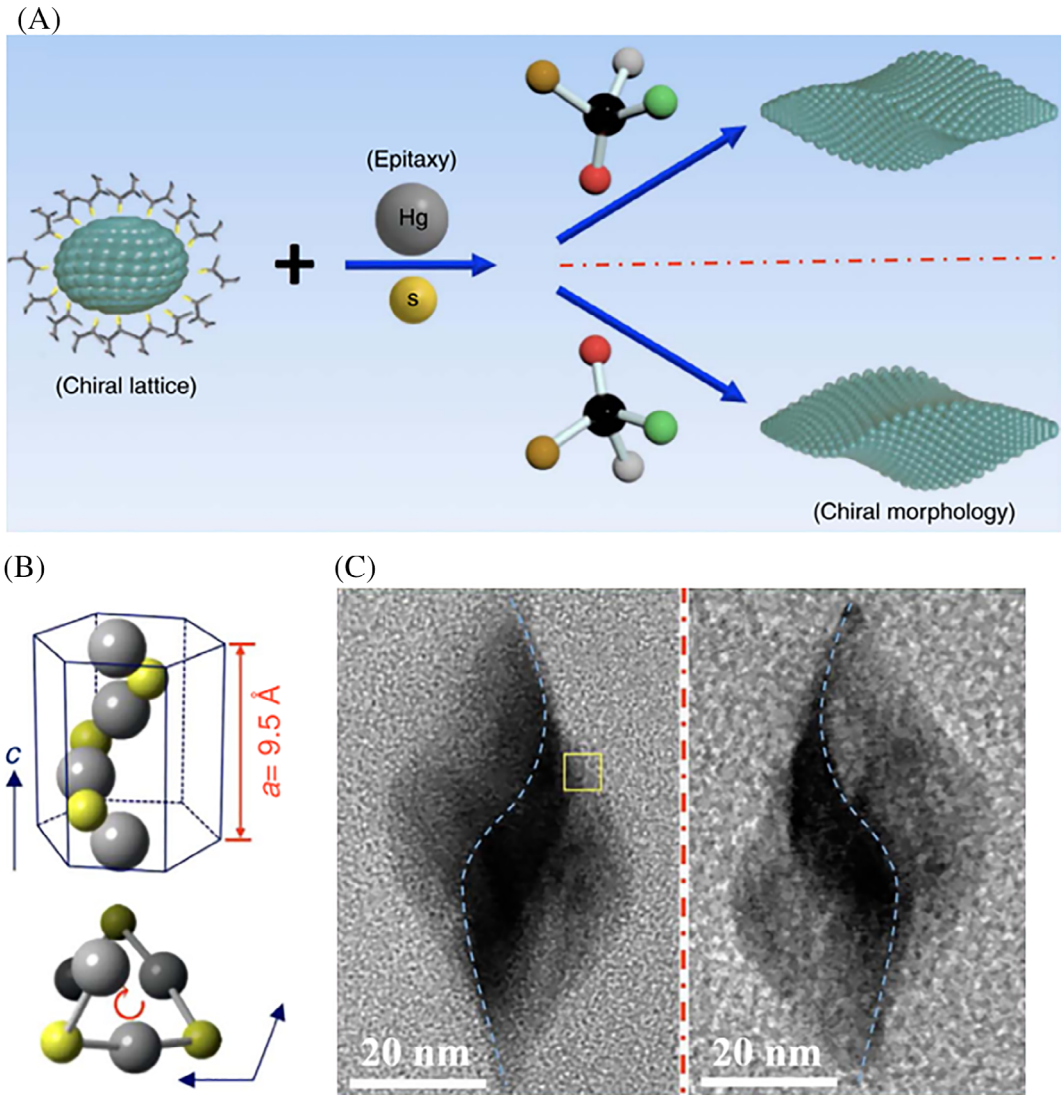

FIGURE 5 (A) Schematic of the growth process based on epitaxial principle with involvement of chiral molecules to tailor the chirality of morphology; (B) atomic model of cinnabar HgS lattice along crystallographic *c* axis, showing helical arrangement of atoms. The top image shows the side view, and the bottom image shows the top view. Gray and yellow spheres are Hg and S atoms, respectively; (C) TEM images of right-handed (left image) and left-handed (right image) as-synthesized α-HgS nanostructures made by the synthetic route in (A). The average length and aspect ratio of nanostructures in both samples are 76.9 ± 5.8 nm and 1.90 ± 0.15, respectively. Blue dashed curves are added to guide the eyes for different twisting orientation in nanostructures. Adapted with permission from Ref. 58 Copyright © 2017, Springer Nature

were compared to those of α-HgS nanostructures, which also possessed crystallographic chirality but had achiral morphologies (nanocubes, nano-ellipsoids, nanorods, and nanowires), revealing that the optical activity of α-HgS nanostructures with achiral morphologies originated from the chiral crystal lattice. At the same time, the chiral morphology of twisted triangular bipyramids could induce an additional CD response in the UV–Vis spectral range, which is qualitatively related to the characteristic length of the twisted shape. Thus, a suggested synthetic mechanism allows the control of crystallographic and geometric chirality of nanocrystals, tailored to different length scales. In turn, this opens new horizons for studies of cooperative chirality in various inorganic systems, including NP assemblies.

To create morphologies of semiconductor core/shell superstructures so they could be applied in a wide range of cases, a thermodynamically controlled growth regime is needed. For example, the morphology of ZnS shells deposited on ZnSe nano rods could be tuned from flat to islands-like by decreasing the shell growth rate[118] (Figure 6A,B). In this case, the interfacial strain energy is also decreased. Further reduction of growth speed up to thermodynamic limit could lead to the formation of helical-shell morphology, which minimizes the sum of the strain and surface energy. Unlike the other morphologies, ZnSe/ZnS nanorods with helical shells maintain bandgap emission (Figure 6C). As-synthesized ZnSe/ZnS nanorods, even with helical shells, did not show any CD in dispersions, which is likely due to racemic composition of the ZnS shells. However, optical activity was induced in these nanorods by replacing initial nanorods ligands with chiral *D*- and *L*-Pen molecules (Figure 6C). In this case, optical activity appeared due to the interaction of the surface zinc

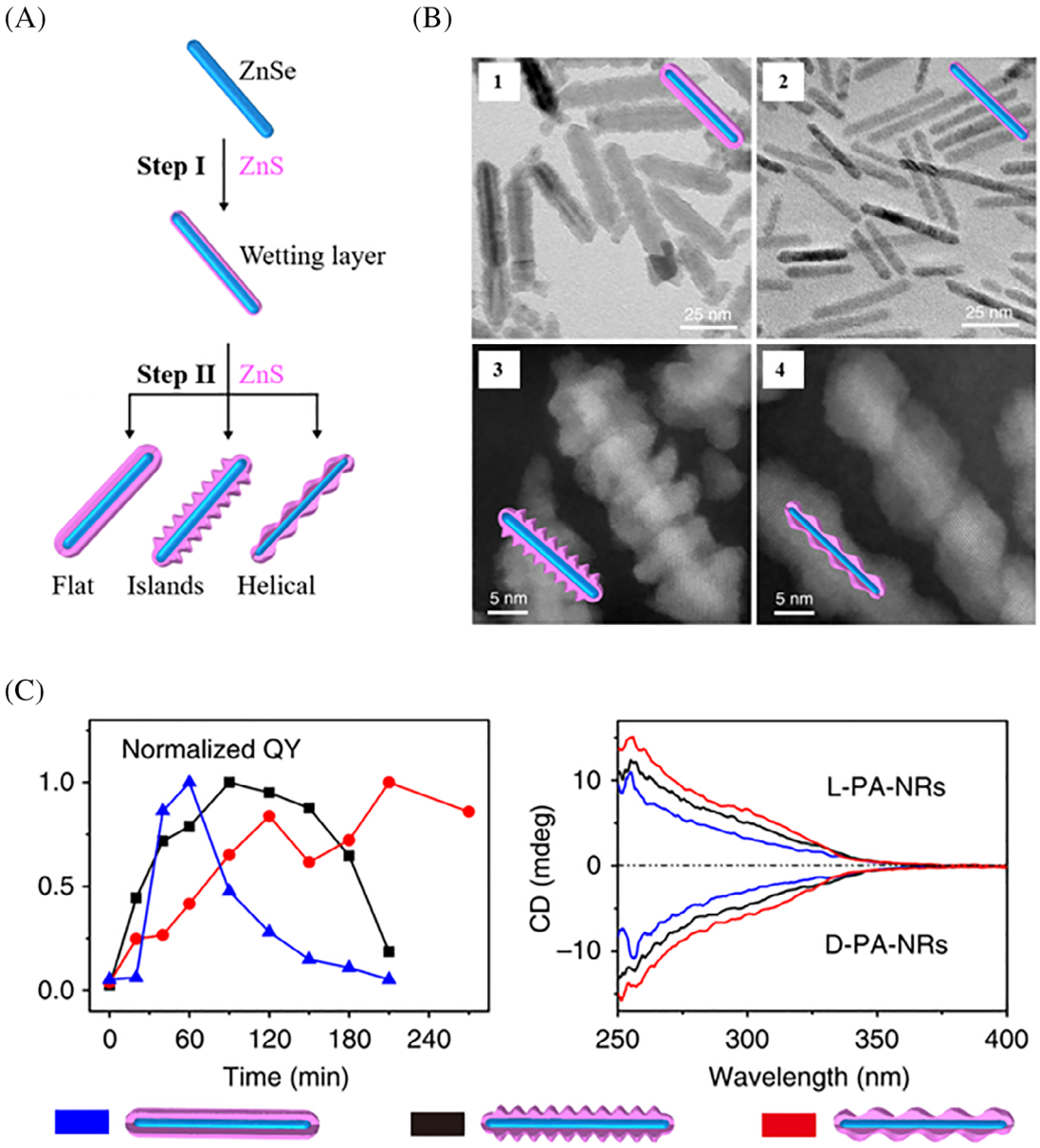

FIGURE 6 (A) Schematics of the controlled shell growth of ZnS on a ZnSe nanorod. Step I: initial uniform ZnS shell growth when below critical thickness. Step II: further ZnS growth leads to flat-, islands- and helical-shell morphologies by controlling the ZnS growth rate via tuning the precursor reactivity; (B) 1—TEM image of ZnSe/ZnS core/flat-shell nanorods in Step II; 2—TEM image of ZnSe nanorods with thin uniform ZnS shell before islands growth starts; 3—high-resolution high angle annular dark field (HAADF) scanning TEM (STEM) images of ZnSe/ZnS core/islands-shell nanorods in Step II; 4—high-resolution HAADF STEM images of ZnSe/ZnS core/helical-shell nanorods in Step II; (C) left: normalized emission quantum yield. The normalization is performed based on the respective highest values; right: CD spectra after chiral ligand exchange. The core/shell nanorods samples were transferred to water by using *L*- and *D*-Pen. Adapted with permission from Ref. 118 Copyright © 2019, The Author(s)

atoms with Pen.[100] While the shape of CD spectra was similar for ZnSe/ZnS nanorods of different morphologies, the helical-shell ones manifest the highest CD values.

Mixed micelles adsorbed on gold nanorods could form quasihelical patterns that direct seeded growth into NPs with pronounced morphological and optical handedness (Figure 7).[119] Tomography reconstructions (Figure 7D) allowed to establish NPs surface topography, and selected orthoslices show the growth of wrinkles from the gold nanorod seeds and the internal structure of the wrinkle network. The *g*-factors of these structures were size-dependent and ranged from 0.1 to 0.2 (Figure 7F), which are among the highest values reported for colloidal plasmonic NPs in the Vis and NIR spectral range.

The effect of the Cys concentration on chiral distortion was demonstrated for chiral plasmonic nanostructures based on a rhombic dodecahedron shape[116] (Figure 8A). The increase of Cys concentration from 0.1 mM to 0.15 mM was accompanied by, first, a translational shift of the fourfold edge from the central line and, second, a generation of bent edge that deviated from the central line. The 0.2 mM Cys concentration led to significantly curved arms. These highly curved edges resulted in a strongly enhanced CD spectrum

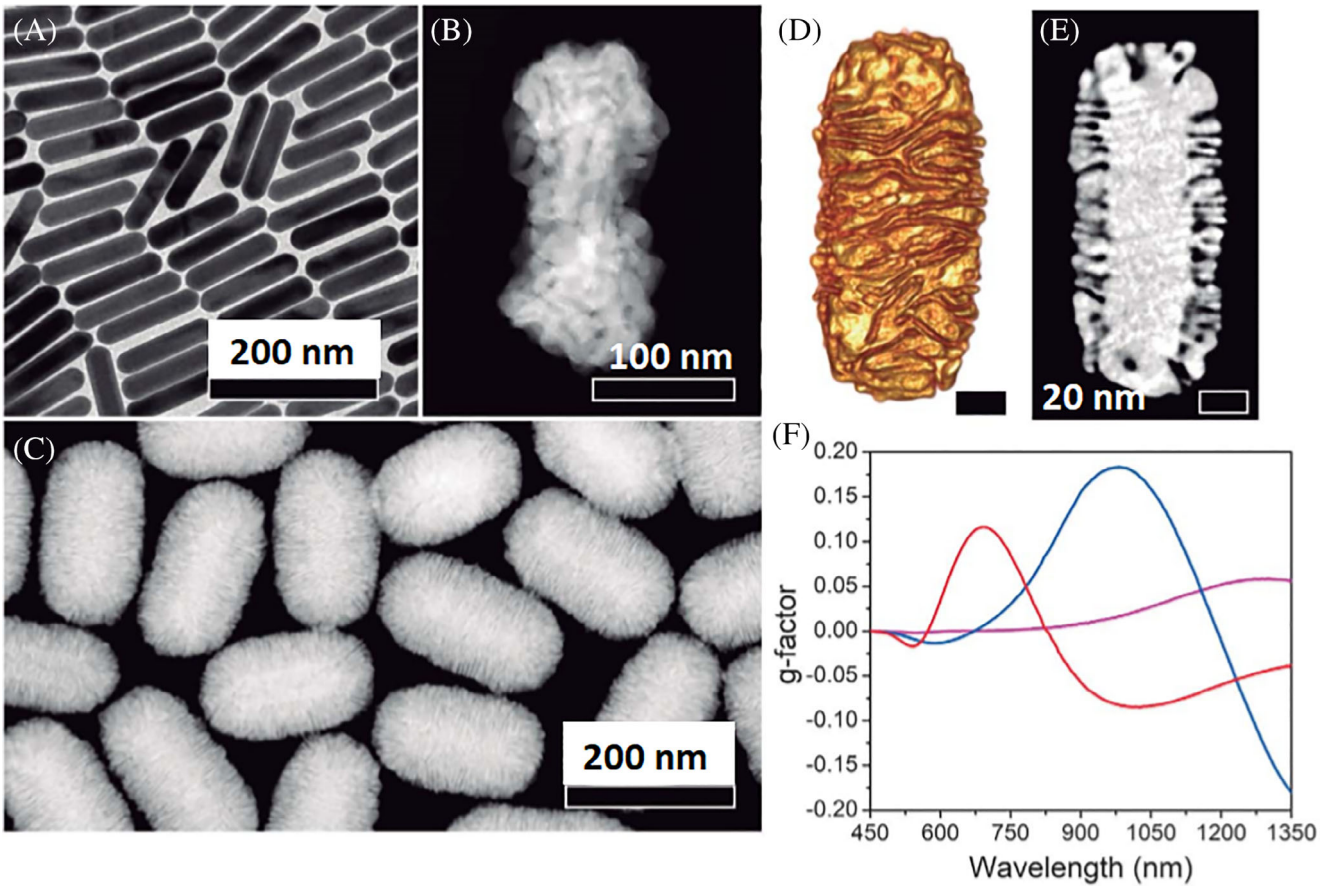

FIGURE 7 (A) TEM image of gold nanorods 130 nm in length and 29 in width used as seeds. (B) High-magnification HAADF-STEM image of a chiral gold nanorod grown in (R)-BINOL displaying a complex surface containing wrinkles. (C) HAADF-STEM image at low magnification of gold nanorods obtained in the presence of (R)-BINAMINE displaying a complex surface containing sharp wrinkles. Gold nanorods of 165 × 73 nm (D,E), grown in (R)-BINAMINE-surfactant mixtures were analyzed by HAADF-STEM. (F) Spectral evolution of the anisotropy factor for chiral gold nanorods with increasing particle size: 165 × 73 nm (red), 210 × 112 nm (blue), and 270 × 175 nm (magenta). Adapted with permission from Ref. 119 Copyright © 2020 The Authors, some rights reserved

with the highest *g*-factor of 0.02, which is almost 10 times larger than that observed for the NPs made with 0.1 mM Cys. Simulations of this system revealed that the noticeable chiroptical property originated from the high-order mode plasmon oscillations. However, further increase of Cys concentration to 0.3 mM led to overgrown edges characterized by the considerable decrease of CD of the NP dispersions, which was associated with increased randomness in helicity of the nanostructures. For NPs viewed along the <111> direction, a random direction of bending was observed due to the uneven growth of chiral edges that were connected. These convoluted edges were expected to be the reason for the decreased CD signal. Also, at high Cys concentrations, the interaction of Cys with the metal surface interfered, resulting in reduced enantioselectivity and the formation of random arms,[59] which innevitably decreases CD intensity.

The strong effect of AA concentration on the morphological development of gold nanostructures with outspreading petal shape is demonstrated in Figure 8B. Note also that the same synthetic parameter also changes the ability of NPs to self-assemble and for complex superstructures via non-classical crystallization pathways.[120] Different concentrations of AAs were shown to change the reduction rate of gold ions. When the concentration of AA was low (0.5 mM), the growth of branched structures with short (~150 nm) and broad (~100 nm) curly petal-like structures complex mesoscale assemblies were observed. The number of these branches was relatively small, implying that the protrusion trend in NP growth is small when the concentration of AA is low. When the AA concentration is increased (10 mM), the development of branched rods with elongated features as well as an increased number of branches were observed. The length and width of each branched rod were about 200 and 40 nm, respectively. Notably, the branched rod was faceted with a twisted pillar structure in the clockwise direction, which corresponded to a right-handed configuration. Thus, high AA concentration provides fast kinetic growth, which, in turn, results in twisted pillar structures. The authors noted that according to the literature, under the fast reduction kinetic condition, branched structures are mainly synthesized due to the facilitated deposition rate of the metal atoms.[121,122] At the same time, reduced kinetics produces a broadly curved surface. These results demonstrate that the deposition rate of gold atoms mediated by AA concentration could influence the growth of branched nanostructures and modulate their curved petal geometry in accord with chiral preferences of NP-NP interactions.[123]

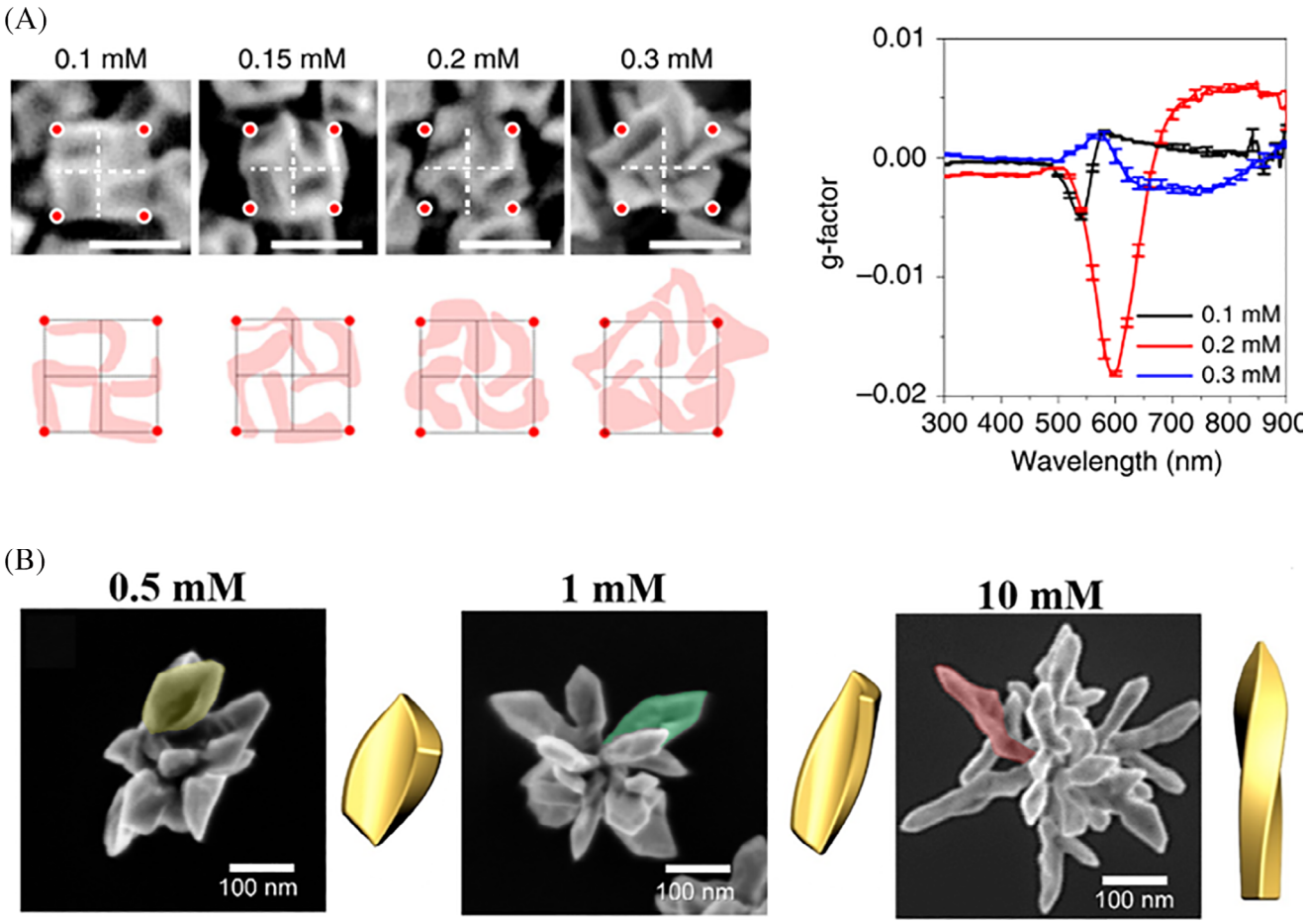

FIGURE 8 (A) Left: SEM images of Au NPs under different Cys concentrations ranging from 0.1 to 0.3 mM. The particles are aligned with the same <100> orientation. The centerlines (white dashed lines) and corners (red dots) of the NPs are displayed in the SEM images to clearly show the deviation of the edges from the centers. The highlighted edges of each NP are represented at the bottom of the SEM images, and the edge deformation is directly compared based on the same black standard lines. Scale bars, 100 nm; Right: the *g*-factor spectra of NPs prepared with different Cys concentrations. Adapted with permission from Ref. 116 Copyright © 2020, Springer Nature; (B) the effect of AA concentration ranging from 0.5 to 10 mM on the morphological development of gold NP. Corresponding models of petal geometry are shown in right panels. Adapted with permission from Ref. 117 Copyright © 2015, Royal Society of Chemistry

4.2 | Assembly of chiral nanostructures using biological interactions

Biomolecules (DNA, peptides) are widely used for the preparation of chiral inorganic nanostructures. Biomolecule-mediated chiral nanostructures have been comprehensively discussed in several reviews.[17,24,28,124,125] Here, we will only briefly discuss the chirality engineering method specific to the biomolecules. Note that for many of them, the same mechanisms, such as the ligand effect, are still applicable when NPs are synthesized in the presence of biomolecules, such as the case with Ag NPs grown on the chiral poly(dG)-poly (dC).[126] TEM analysis of Ag NPs grown on the DNA template revealed a large number of twinning defects indicative of the transfer of chirality from the surface of the NPs to its inorganic core.

What is special about the biomolecular approach to the engineering of chiral structures is that one can reliably make nanostructured assemblies with nano-, meso-, and microscale chirality from achiral and racemic components using the specificity of biomolecular interactions. Sometimes the terms "structural," "geometric," or "extrinsic" chirality are used to describe nanostructures whose assembly is guided by the biomolecules. Although these terms are tautologies or misnomers in the context of chiral structures, they nevertheless convey an important point that the observed optical properties are related to the mirror asymmetry of NP collection overall rather than their individual geometries or electronic effects at their interface.

Starting from the DNA-driven assemblies made by polymerase chain reaction (PCR) where strong CD peaks were observed but the actual assemblies were the mixture of dimers, trimers, and tetramers (Figure 9A),[62] the well-recognized chiral shapes with pyramidal (Figure 9B)[63] and helical (Figure 9C,D)[127,128,130] placement of NPs in 3D space were obtained. More intricate assemblies of nanorods pairs with scissors-like,[129] (Figure 9E,F) and propeller-like geometry were obtained[131] using hybridization of designer DNA strands that is often referred to as DNA origami. Note that this type of chiral assembly is

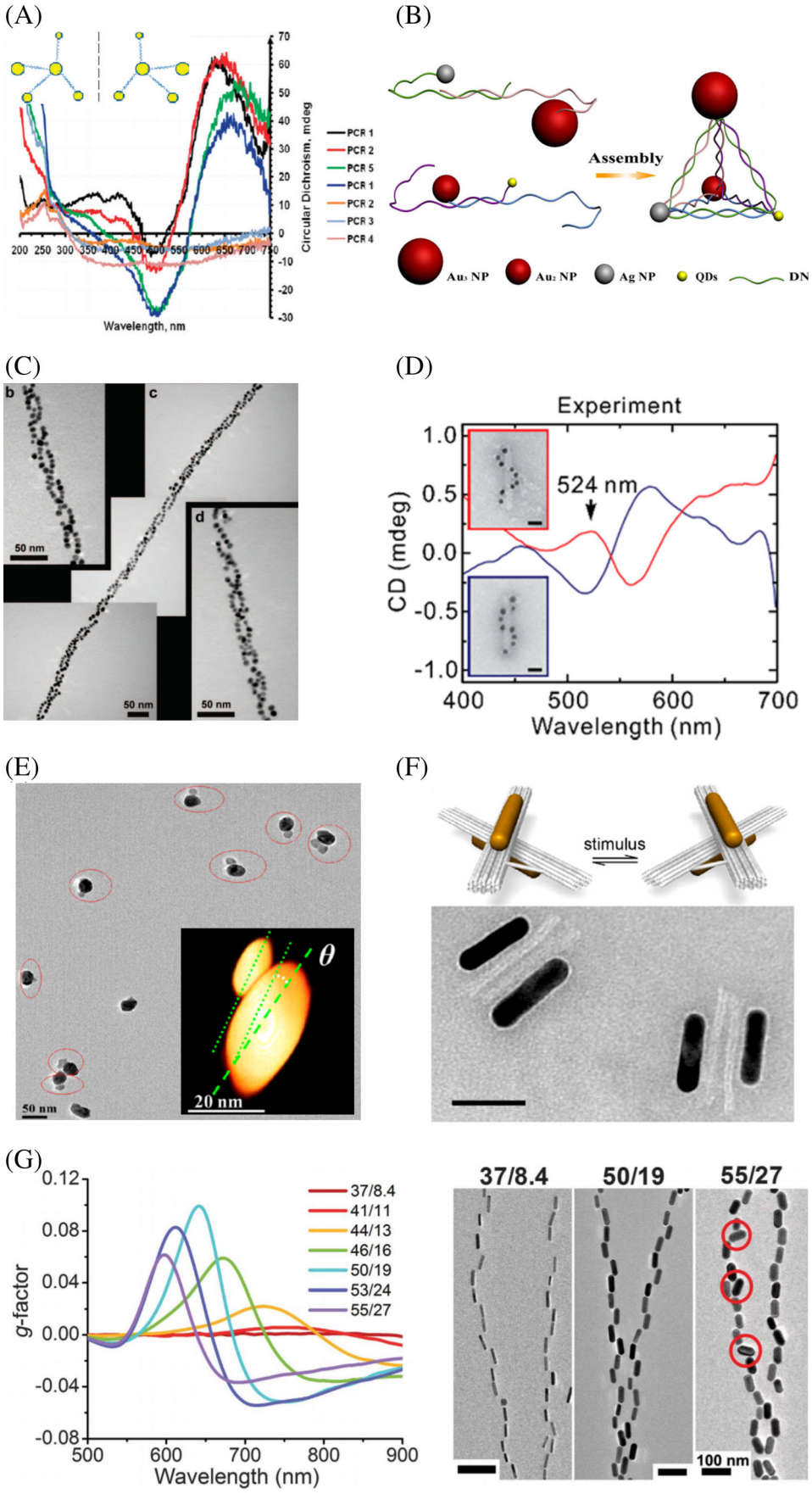

FIGURE 9 (A) Schematics of chiral NP superstructures (top) and CD spectra of products of PCR for increasing number of cycles (bottom). Adapted with permission from Ref. 62 Copyright © 2009 American Chemical Society. (B) Scheme of the synthesis of chiral NP pyramid. Reproduced with permission from Ref. 63 Copyright © 2012 American Chemical Society. (C) TEM images of Au NP double helices. Adapted with permission from Ref. 127 Copyright © 2008 American Chemical Society. (D) Plasmonic helices created by arranging Au NPs on origami bundles and the measured CD spectra. Reproduced with permission from Ref. 128 Copyright © 2012 Nature Publishing Group. (E) Representative TEM images of the assembled Au and Ag NPs heterodimers made using antibody–antigen bridges. The insert shows their TEM tomography image. Adapted with permission from Ref. 129 Copyright © 2013 American Chemical Society. (F) Plasmonic nanostructures with dynamically controlled optical responses enabled by stimulus-driven DNA origami templates. Reproduced with permission from Ref. 125 Copyright © 2018 American Chemical Society. (G) g-factor spectra and representative TEM images for helices from various sizes of NRs assembled under identical conditions. The numbers in the legends, for example, 37/8.4, represent the average length (37 nm) and diameter (8.4 nm) of the NRs. Adapted with permission from Ref. 103 Copyright © 2021 The Authors, some rights reserved; exclusive licensee American Association for the Advancement of Science

known for strong CD but not for high values of the *g*-factors because their optical asymmetry is limited by strong scattering. Recently it was shown that these limitations could be eliminated by the long-range organization of nanorods in a manner similar to the liquid crystals.[103] Helices obtained by self-assembly of ~35 gold nanorods driven by the affinity of polypeptides (Figure 9G) increased optical asymmetry of individual nanorods by 4600 times leading to the cumulative *g*-factors of ~0.12.

4.3 | Non-classical growth of chiral crystalline nanostructures

A mechanism of non-classical crystallization is oriented attachment (OA),[132,133] during which particles spontaneously assemble by first aligning along a common crystallographic orientation and then merge to create a crystallographically coherent interface.[134–137] From a thermodynamic point of view, OA leads to a decrease in the surface energy of primary particles when they merge into a single crystal.[138]

The steps involved in OA have been well-established through high-resolution transmission-electron-microscopy (HRTEM) imaging.[139,140] Penn and Banfield reported OA for assembly of titanium dioxide nanocrystals[141,142] and nanocrystalline iron oxyhydroxides,[143] while Kotov and coworkers independently reported it for CdTe NPs.[133] These studies were followed by similar observations for ZnO and Mn-doped PbSe NPs.[144,145]

OA can be mediated by many factors, including the shape, faceting, and the ligand coverage of NPs,[146] giving rise to perfect interfaces.[147] However, in some cases, incoherent interfaces have been observed.[140,142,148] In particular, HRTEM revealed dislocation formation during early growth that involved attachment between two or more TiO_2 NPs[142] (Figure 10A). Since the initial NPs were defect-free, the dislocation appearance was attributed to the growth process itself. Thus, even a small misorientation in the interface during the particle growth, known as imperfect OA, can result in NPs with screw dislocations. Also, $b = a/2[110]$ edge dislocations occur as a result of the imperfect attachment of PbTe NPs on both {100} and {110} facets (Figure 10B).[147] In addition to screw and edge dislocations, twins and stacking faults can also break the symmetry of the crystal. As shown in Figure 10C, asymmetric one-dimensional silver cones grown by OA exhibited mixed twins and stacking fault domains along the {111} direction.[149] Other defects also appeared during the organization of single orange- and red-emitting CdTe NPs into crystalline nanowires upon controlled removal of the protective shell of the organic stabilizer (Figure 10D).[133]

It has been recently demonstrated that imperfect OA of lanthanum hydroxide $La(OH)_3$ NPs assembling into highly anisotropic nanosheets was accompanied by multiple surface defects and dislocations (Figure 11A), including point defects, screw dislocations, edge dislocations, tilt and twin boundaries, as well as stacking faults.[150]

Analysis of the OA process between silver (Ag) NPs through molecular dynamics (MD) simulations[151] revealed that the OA between 100 facets of Ag NPs leads to imperfect OA, forming a final structure that is twisted (Figure 11B). These findings indicate that a single type of achiral NP can be involved in the growth of different complex structures, some of which may become chiral.

While there are a number of cases where OA and other types of NP assembly lead to chiral structures, they may not lead to the preferential left- or right-handed nanostructures, where the overall system remains racemic and chiroptically silent. Here we are primarily interested in the processes that lead to chiral preferences in the final structures. For example, α-HgS NPs with well-defined handedness of both crystal lattice and morphology can self-assemble into collinear chains and propellers[152] (Figure 12). The assembly process was induced by silver ions, where the ion concentration determined the type of final structures. While low Ag^+ concentration led to collinear chains, high Ag^+ concentration resulted in the formation of propellers (Figure 12A). Highly collinear chain-like nanostructures were formed using two types of individual NPs, 25 nm long α-HgS nano-ellipsoids that have chiral lattice but achiral morphology (Figure 12B) and 60 nm long twisted triangular bipyramid α-HgS that have both chiral lattice and morphology (Figure 12C). Ag^+ ions selectively attack the ends of nano-ellipsoids that have a low density of capping molecules. The Ag^+ ions then exchange with Hg^{2+} ions on the surface to form soluble Ag_2S, which etched and exposed fresh α-HgS surface for assembly. These {003} facets of α-HgS are terminated with either Hg or S, which in turn leads to a polar surface with large dipole moments along the [001] axis (Figure 12B). Thus, seamless straight-chain superstructures were assembled via an OA mechanism, driven by both large longitudinal dipole moments and new facets. The same mechanism was seen for the assembly of twisted triangular bipyramid α-HgS (Figure 12C). A high concentration of Ag^+ ions used for the assembly of bipyramid resulted in propeller-like nanostructures (Figure 12D), in which three or four bipyramids cross-linked and coalesced with a spherical domain feature in the center, which was an alloy of $Hg_{0.64}Ag_{0.36}S$. These structures were formed by a different mechanism compared to that of collinear chain-like assemblies. In particular, self-assembly of the structures with continuous crystallinity was shown to take place for the assembly of propeller-like nanostructures. This process occurred due to the formation of an eutectic mixture of Ag_2S and HgS when the concentration of Ag^+ ions increased (Figure 12A). This leads to the deformation and recrystallization at the ends of bipyramids, thus activating and promoting linkage of bipyramids under steric hindrance. The chain-like assemblies appeared to be optically active in a UV–Vis spectral range (Figure 12E). CD peaks of building blocks and their chains are the same around 540 nm and different below 500 nm. Therefore, CD bands around 540 nm correspond to the chiral crystal lattice, while CD bands less than 500 nm relate to the interplay between chiral morphology and chiral lattice.[58] Thus, chiroptical properties on nanostructures can be carefully tuned by varying chirality of crystal lattice and morphology of their building blocks.

4.4 | Light-induced chirality transfer

Left- and right-handed CdS/CdTe nanoribbons can be formed with equal probability under the illumination of unpolarized light.[153] At the same time, illumination of dispersions of CdTe NPs of a truncated

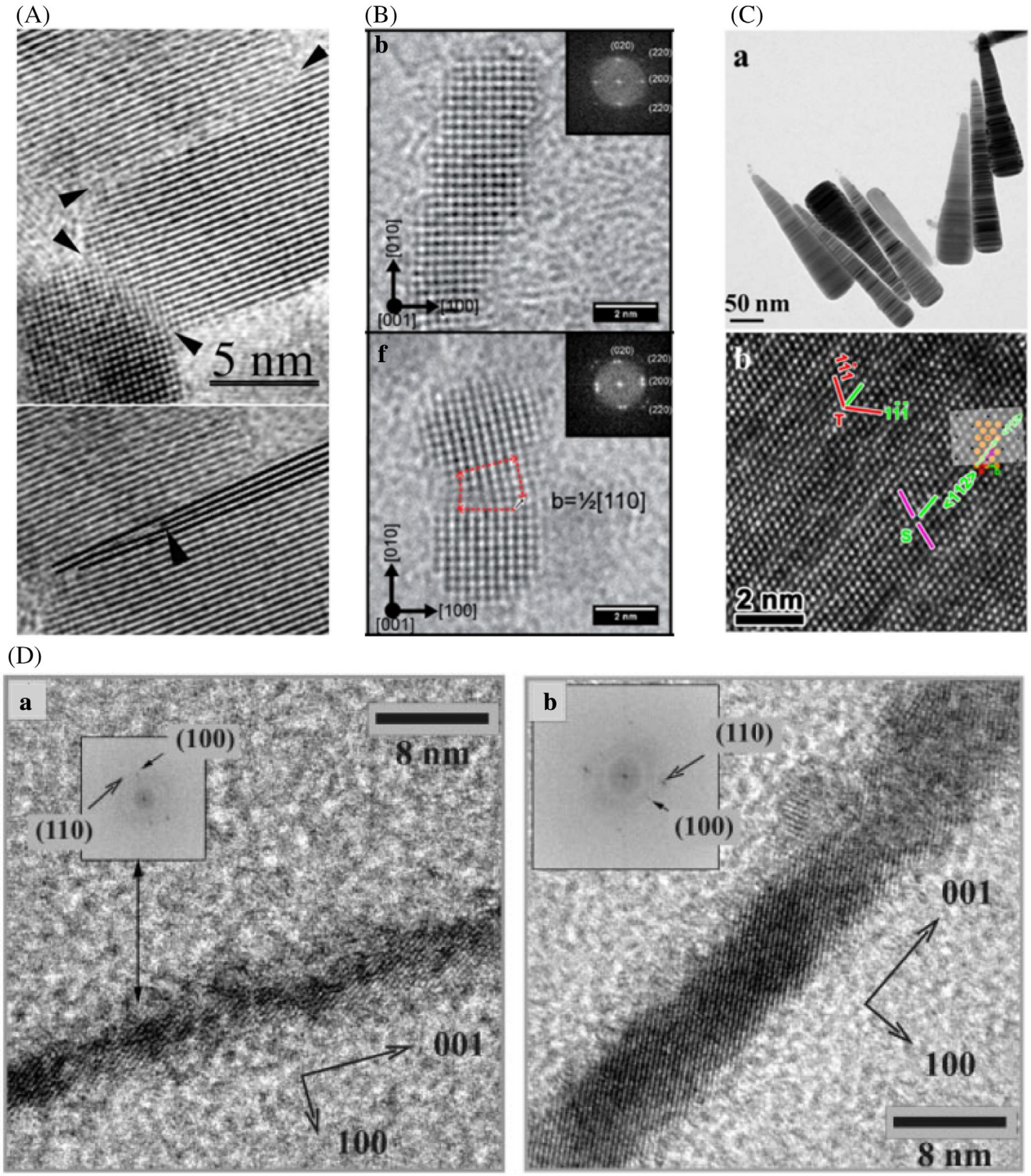

FIGURE 10 (A) HRTEM image of three attached TiO_2 particles. Arrowheads mark interfaces between primary NPs. The edge dislocation at the upper interface is reproduced below, with lattice fringes around the terminating plane (arrowhead) highlighted for clarity. Adapted with permission from Ref. 142 Copyright © 1998, The American Association for the Advancement of Science. (B) Top: experimental HRTEM image and corresponding FFT of three PbTe NPs that have attached perfectly on the {100} facets. Bottom: Experimental HRTEM image and corresponding FFT of PbTe NPs attached imperfectly on {100} facets with a b = a/2 [110] Burgers vector. Red dotted arrows outline the Burgers circuit with the Burgers vector shown with a white outlined black arrow. Adapted with permission from Ref. 147 Copyright © 2018 American Chemical Society. (C) TEM image (top) and HRTEM image (bottom) of the center part of an individual silver cone. Twins and stacking faults are designated as T and S, respectively. Adapted with permission from Ref. 149 Copyright © 2013 American Chemical Society. (D) High-resolution TEM of nanowires made from (a) orange- and (b) red-emitting CdTe quantum dots. Reproduced with permission from Ref. 133 Copyright © 2002, The American Association for the Advancement of Science

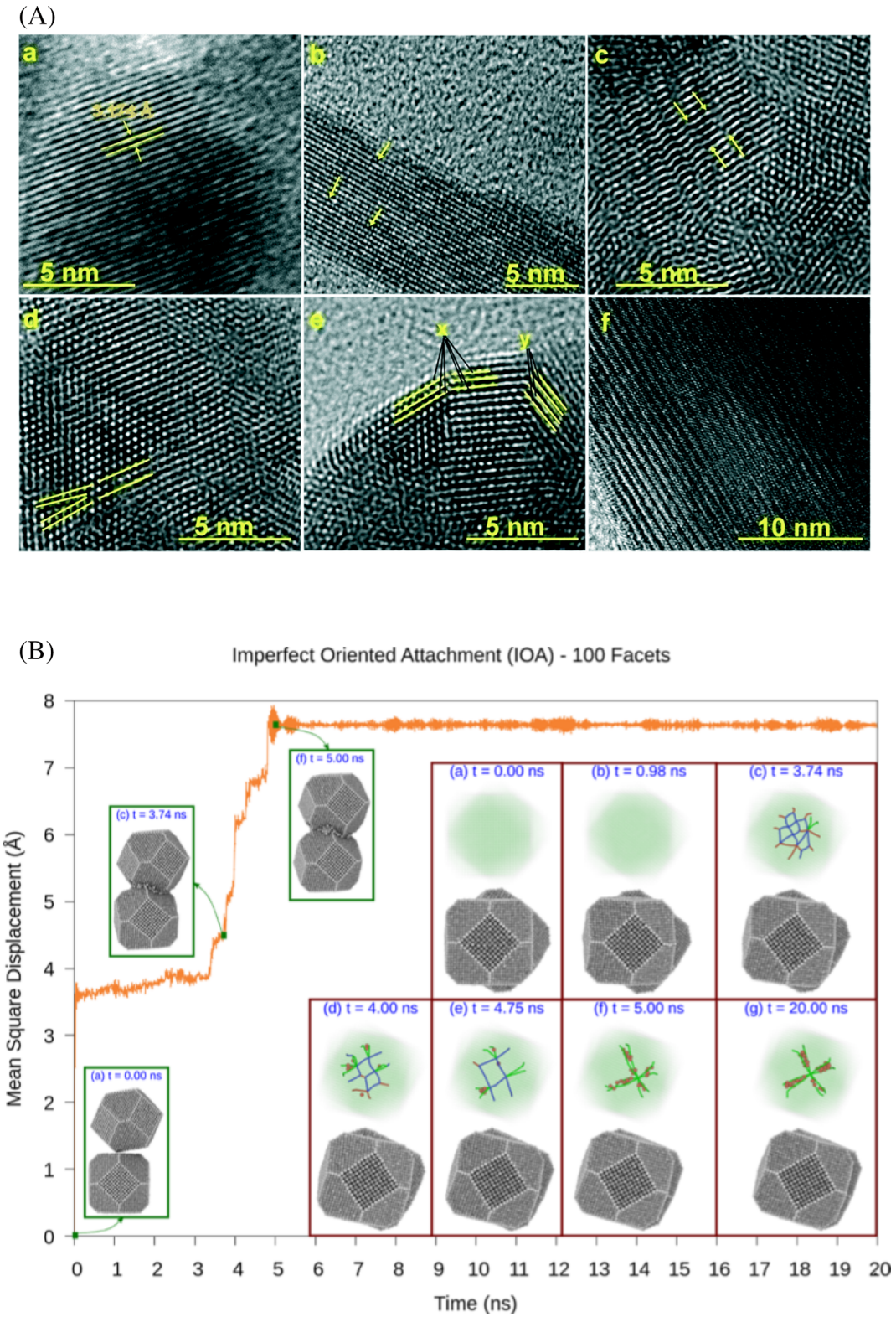

FIGURE 11 (A) (a) Lattice fringes of $La(OH)_3$ NPs, (b) point defects in $La(OH)_3$ nanosheets, (c) screw dislocations in $La(OH)_3$ nanosheets, (d) edge dislocations in $La(OH)_3$ nanosheets, (e) tilt and twin boundaries in $La(OH)_3$ nanosheets and (f) stacking faults in $La(OH)_3$ nanosheets. Reproduced with permission from Ref. 150 Copyright © Royal Society of Chemistry. (B) Role of dislocation emergence and evolution during the crystallization process of an Ag NP dimer interface along the 100 facets. In the visualizations, the all-atom view is accompanied by a filtered image in which all atoms, except the hcp ones, are made translucent. Blue ribbons indicate perfect, 1/2 ⟨110⟩ dislocations. Green ribbons indicate 1/6 ⟨112⟩, Shockley partials. Red ribbons indicate unstable dislocations. At 20 ns, one node centered at the middle of the interface from which Shockley partial dislocations emerge in the contact plane spawns four hcp stacking faults that stabilize the structure in a lightly twisted imperfect OA. Reproduced with permission from Ref. 151 Copyright © 2021 American Chemical Society

tetrahedron shape and stabilized by the achiral TGA molecules, with right- and left-handed CPL with a wavelength of 543 nm led to the formation of right- and left-handed twisted nanoribbons, respectively.[31] These ribbons have mirror-imaged CD spectra with *g*-factors ~3 × 10^{-5}. Due to the truncated tetrahedron shape, the dispersion of CdTe NPs was a racemic mixture. When this NP racemate was irradiated by left- and right-handed CPL, left- and right-handed NPs, respectively, absorbed light more effectively. Then, TGA ligands of photoactivated NPs underwent photooxidation, which transformed CdTe NPs into ligand-free CdS NPs. In turn, these bare NPs assembled into twisted nanoribbons, where the helicity resulted from the chirality of individual building blocks. Interestingly, the enantiomeric excess (an imbalance of the quantity of right and left enantiomers in a mixture) of nanoribbons was about 30%. Enantiomeric excess is determined by the equation: ee = (R − S)/(R + S), where R and S are the concentrations of right- and left-handed enantiomers in a mixture, respectively. This is much higher than that of a 0.5%–2% enantiomeric excess in organic reactions stimulated by light.[154] In another recent work, CPL induced a photochemical reaction in CdSe/ZnS NPs, which led to the appearance of mirror-image CD signals in initially chiroptically inactive NPs.[34]

Along with semiconductor NPs, plasmonic nanostructures can also be made optically active under CPL illumination. In particular, CPL could make ~2 nm gold NPs assemble into chiral nanostructures with complex shapes and dimensions of ~10–15 nm. Even though the nanostructures formed under left-handed and right-handed CPL were complex in shape and were not perfect mirror images of each other, their CD spectra were mirror-imaged, and *g*-factors were reaching up to ~5 × 10^{-5}. This phenomenon was related to the asymmetric displacement of NPs in dynamic assemblies by plasmonic fields followed by OA of NPs. In other work, light-induced

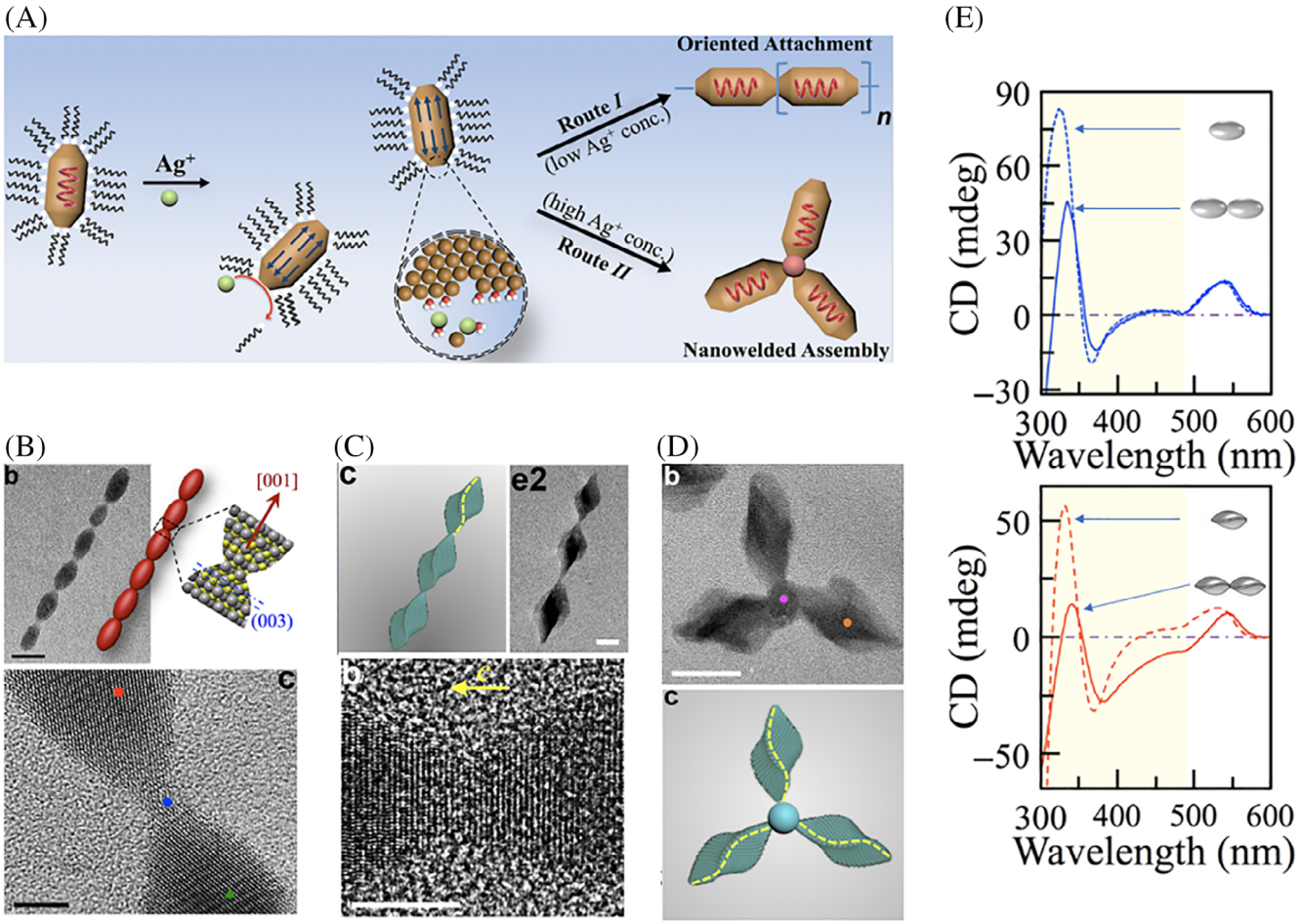

FIGURE 12 (A) Schematic illustration assembly of chiral α-HgS nanocrystals into collinear chains and propellers assisted by Ag ions; (B) Top: TEM image and structural model of a collinear chain assembled from six α-HgS nano-ellipsoids. Scale. Scale bar, 25 nm. Bottom: HR-TEM image of the interconnection between two nano-ellipsoids in a chain. Scale bar, 5 nm; (C) Top: model and TEM image of a chain assembled from three left-handed twisted triangular bipyramid α-HgS. Scale bar, 20 nm. Bottom: HR-TEM image of the interconnection between two bipyramids in a chain. Scale bar, 5 nm; (D) TEM image (top) and model (bottom) of a propeller-like nanostructures assembled from left-handed twisted triangular bipyramid α-HgS. The three blades and central domain are pure HgS and alloyed $Hg_{0.64}Ag_{0.36}S$, respectively; (D) Experimental CD spectra of building blocks (dashed line) and their assembled chains (solid line) for the nano-ellipsoids (top) and twisted bipyramid (bottom) building blocks, respectively. Adapted with permission from Ref. 152 Copyright © 2017 American Chemical Society

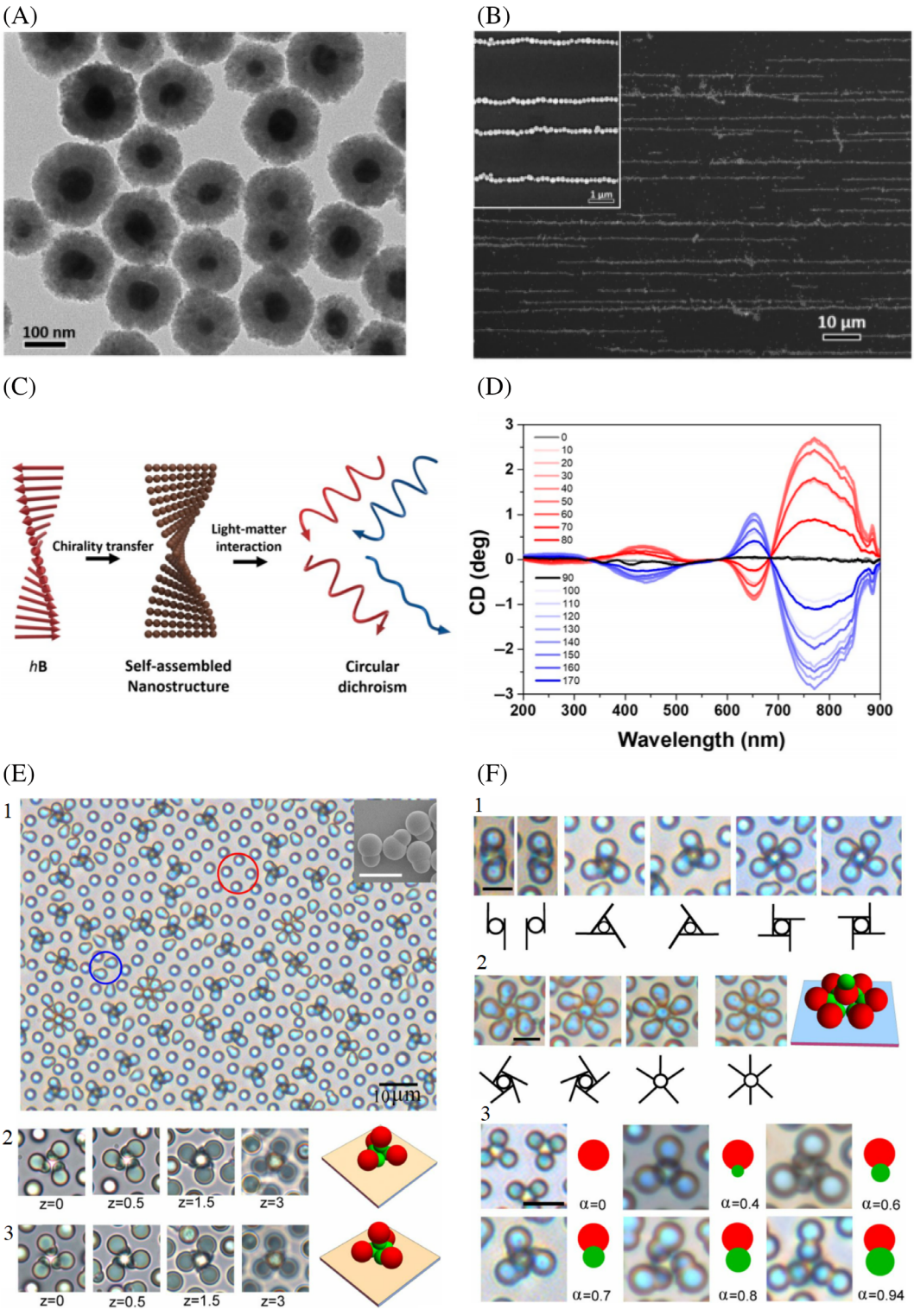

FIGURE 13 (A) TEM image of $Ag@Fe_3O_4$ NPs; (B) SEM image of nanochain structures assembled from $Ag@Fe_3O_4$ NPs. The inset shows the magnified image; (C) scheme of *h***B**-induced chiroptical property; (D) CD spectra of assembled $Ag@Fe_3O_4$ superstructures with varying θ ($0^\circ \leq \theta < 180^\circ$). Color legend depicts the handedness of the magnetic field: left-handed is red, right-handed is blue. Adapted with permission from Ref. 156 Copyright © 2020 American Chemical Society. (E) chiral colloidal clusters assembled from asymmetric dimers under alternating current electric fields (peak-to-peak voltage $V_{pp} = 11$ V and $\omega = 600$ Hz): (1) large field of view of chiral tetramers. The inset shows SEM image of asymmetric dimer building blocks. (Scale bar: 5 μm.) (2 and 3) z-scans (unit: micrometers, moving away from the bottom substrate) of the right- and left-handed chiral tetramers, respectively; (F) The chirality depends on both the geometry and orientation of dimers: (1) chiral clusters (trimer, tetramer, and pentamer) with an increasing number of petals. The central dimer orients its small lobe toward the substrate. (2) chiral/achiral clusters with five and six petals. The central dimer orients its large lobe toward the substrate. (3) colloidal tetramers formed from dimers with different aspect ratios, $\alpha = R2/R1$. (Scale bars for 1–3: 5 μm). Adapted with permission from Ref. 157

chirality in gold nanocuboids, serving as precursors on a semiconductor, by localized electric fields at specific corners of the cuboids depends on the light's handedness and deposited dielectric moieties as electron oscillation boosters by the localized electric field.[33] These studies demonstrate that chirality can also be transferred from light to matter and result in chiroptically active nanostructures with high enantiomeric excess. They also open new horizons to develop large-scale and cost-effective fabrication of chiral nanomaterials and devices based on them.

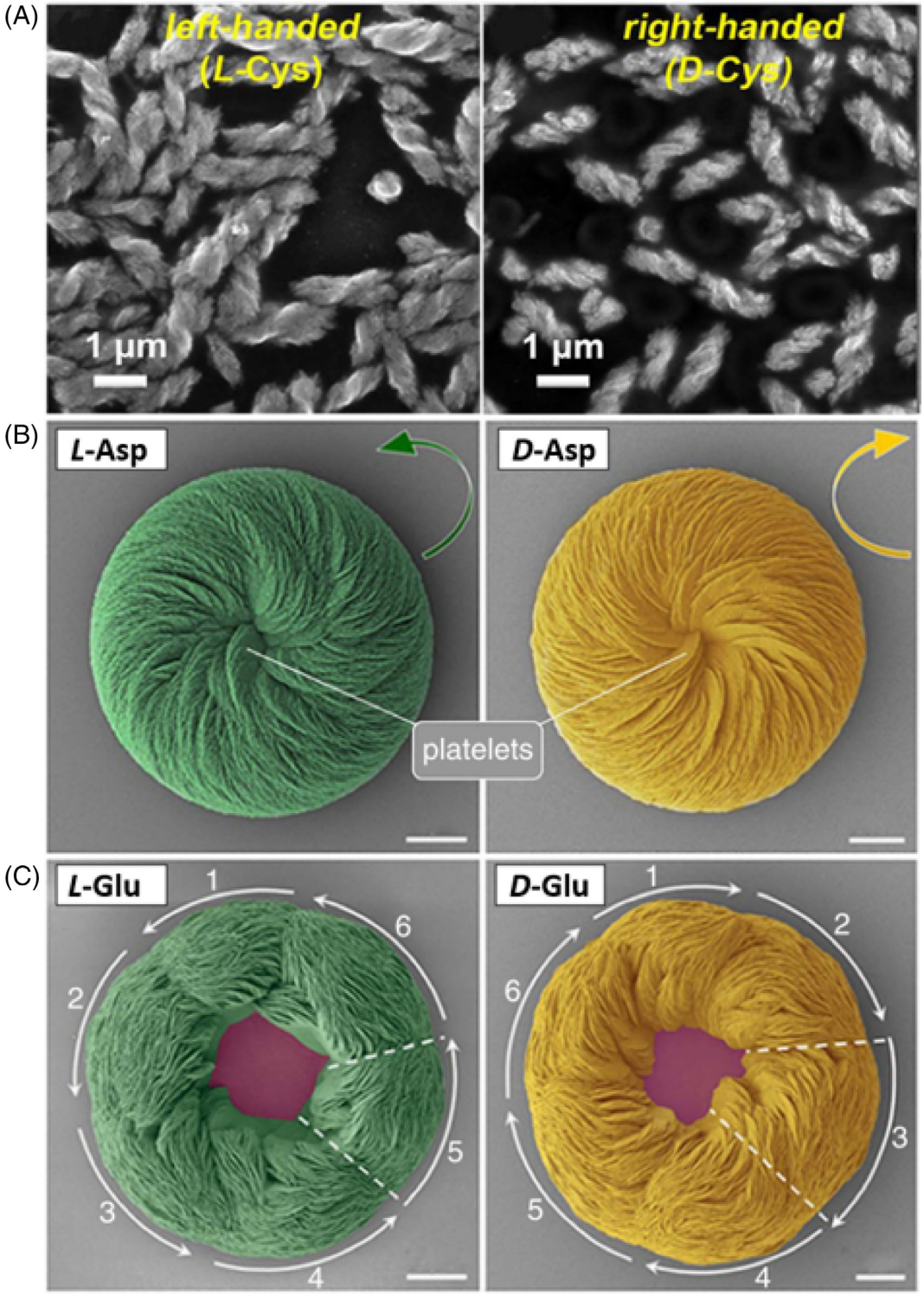

FIGURE 14 (A) SEM images of nanostructured helices made by self-assembly of CdTe NPs *L*-Cys and *D*-Cys surface ligands. Adapted with permission from Ref. 67 Copyright © 2019 American Chemical Society. (B) and (C) pseudo-coloured SEM images of vaterite superstructures grown with the addition of enantiomers of *L*-/*D*-Asp and *L*-/*D*-Glu, respectively. Adapted with permission from Ref. 173 Copyright © 2017, The Author(s)

4.5 | Magnetic and electric fields-induced chirality transfer

Magnetic and electric fields could also serve as driving forces for the assembly of NPs into complex nanostructures. Since an external magnetic field could control magnetic NPs, magnetic layer-by-layer assembly was used to produce asymmetric films and some of them exhibited preferential mirror asymmetry.[155] In particular, Fe_3O_4 or $Ag@Fe_3O_4$ assemblies consisting of hundreds of magnetite NPs (diameter ~10–20 nm) were magnetically aligned into linear nanochains with a high aspect ratio (up to 10^2), that then fixed on the substrate surface through electrostatic attractions.[155] The chirality of the magnetic field could be transferred to the assembled structures. Indeed, the phenomenon of helical magnetic field (*h***B**)-driven symmetry breaking of light was used to induce self-assembly of magnetoplasmonic $Ag@Fe_3O_4$ core-shell NPs (diameter of the Ag core is ~61.4 nm and the Fe_3O_4 shell thickness is ~54.3 nm.) (Figure 13A) into helical superstructures with tailored, tunable, and switchable chiroptical properties in real-time.[156] In $Ag@Fe_3O_4$ NPs, Fe_3O_4 magnetic shell was used to guide plasmonic materials onto the magnetic flux. Due to the polycrystalline structures of the magnetic shell, $Ag@Fe_3O_4$ NPs possess soft ferromagnetic properties and, in turn, could be assembled along the magnetic flux under an applied external magnetic field (Figure 13B). In the case of *h***B**, assembled superstructures could obtain helical configurations (Figure 13C), which are chiroptically active (Figure 13D). CD spectra of assembled $Ag@Fe_3O_4$ superstructures were measured for different rotation angles, θ ($0^\circ \le \theta < 180^\circ$), which represents the angle between the z-axis and the long axis of the magnets used in custom-built modulator for the *h***B** generation. CD spectra demonstrated two strong CD peaks at 650 nm and 770 nm, which correspond to plasmonic resonance wavelengths of $Ag@Fe_3O_4$ NPs. The positions of CD peaks could be manipulated by varying the plasmonic resonance or coupling by controlling the size of the Ag core and magnetic flux density. The handedness of helices could be dynamically switched by the *h***B** at the millisecond level. This study opens the potential for magnetoplasmonics.

Electric fields could also drive the assembly of particles. For instance, an alternating current electric field was used to assemble colloidal polystyrene dimers with asymmetric lobes ($R_1 = 1.27$ μm and $R_2 = 0.89$ μm) (Figure 13E.1) into chiral clusters.[157] These chiral clusters were responsible for unbalanced electrohydrodynamic flow surrounding them and therefore behave as micro propellers, which rotate in opposite directions according to their handedness. Each cluster consists of four dimers, three of which lie on the substrate and form the "petals." Depending on the rotation direction of the petals, tetrameric clusters could be right- and left-handed (Figure 13E.2 and Figure 13E.3, respectively). Clusters with two, three, and four petals could also be formed with almost equal probability of being right-handed and left-handed (Figure 13F.1). The further increase in the number of petals up to five led to only a few chiral clusters. Six petals resulted in only achiral clusters (Figure 13F.2). Central dimer in those clusters orients its large lobe toward the substrate. It was concluded that observed chirality emerges from the geometric asymmetry of dimer particles. Clusters can be assembled from dimers with different aspect ratios (Figure 13F.3). When the aspect ratio was zero (for sphere) and one (for symmetric dimer), achiral clusters were formed. Only intermediate values of aspect ratios led to the formation of chiral clusters. This approach of getting chiral clusters using an electric field could be projected to different asymmetric particles and used to develop micro engines.

4.6 | Self-limited assembly of nanostructures

Stemming from the studies on self-limited growth of electrostatically restricted layer-by-layer assembled multilayer films,[158–163] self-limited assemblies of nanostructures emerged as a new direction in nanoscale research in the last decade, offering rich opportunities for engineering complex geometrical nanostructures.[164–169] Water-

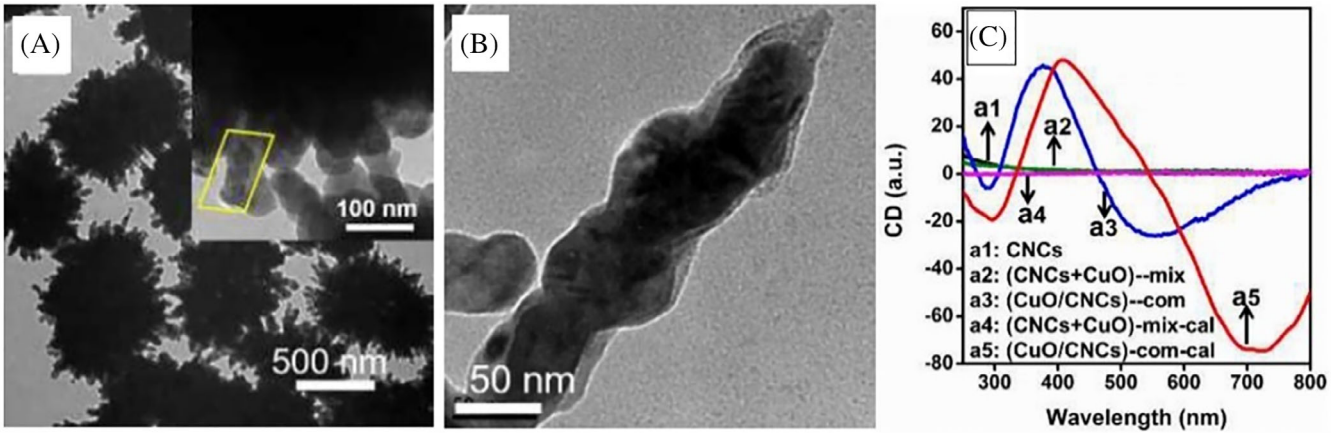

FIGURE 15 (A) TEM images of calcined supraparticles and (B) the nanosheets there are comprised of; (C) CD spectra of CNCs: supraparticles (a3) and calcined supraparticles (a5). The *g*-factor exceed 0.002 for a3 (~380 nm) and 0.005 for a5 (~415 nm). Adapted with permission from Ref. 177 Copyright © 2009, Royal Society of Chemistry

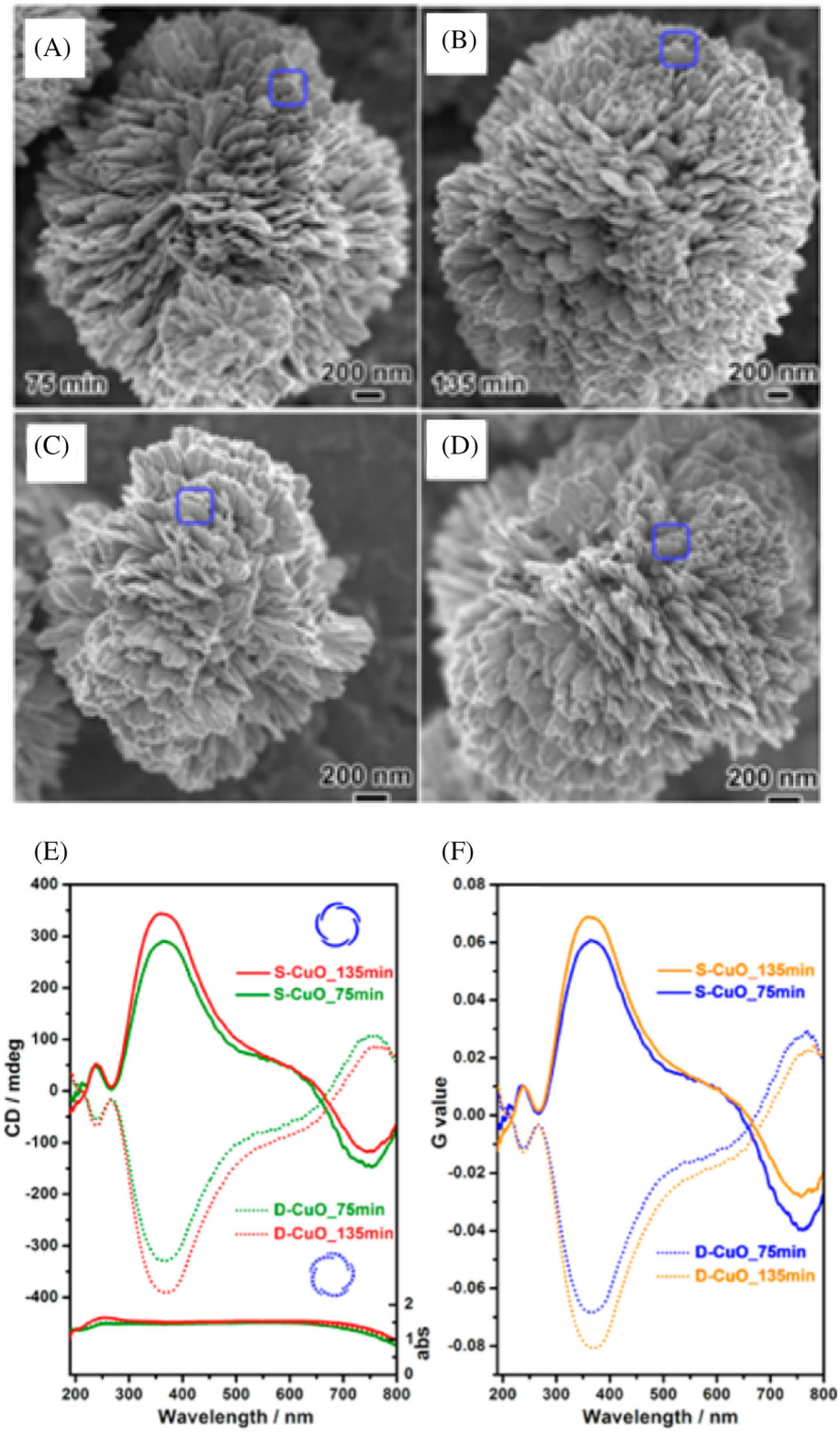

FIGURE 16 (A,B) SEM images of CuO supraparticles synthesized with (*S*)-(−)-2-amino-3-phenyl-1-propanol at synthesis times of 75 min and 135 min; (C,D) SEM images of CuO supraparticles synthesized with (R)-(+)-2-amino-3-phenyl-1-propanol at synthesis times of 75 min and 135 min. (E) DRUV–Vis absorption and DRCD spectra and (F) *g*-factor spectra of the antipodal (S- and D-CuO) chiral CuO supraparticles Adapted with permission from Ref. 175 Copyright © 2014 American Chemical Society

soluble NPs with short capping ligands, such as AAs or dipeptides, have strong electrostatic repulsions and attractions to each other. In this regime, the NPs behave similarly to amphiphilic molecules (e.g., surfactants) and produce micelle-like aggregates termed *supraparticles*.[165] Their size is limited by the repulsive interactions that lead to high uniformity of the supraparticles typically containing 50–300 highly size-polydispersed NPs. Besides various NPs, supraparticles may include proteins and other biopolymers that retain their biological activity,[166,170] while other biomolecules may inhibit it.[171] For instance, CdTe NPs stabilized with 2-(dimethylamino) ethanethiol (DMAET) produce supraparticles with redox-active cytochrome C.[166]

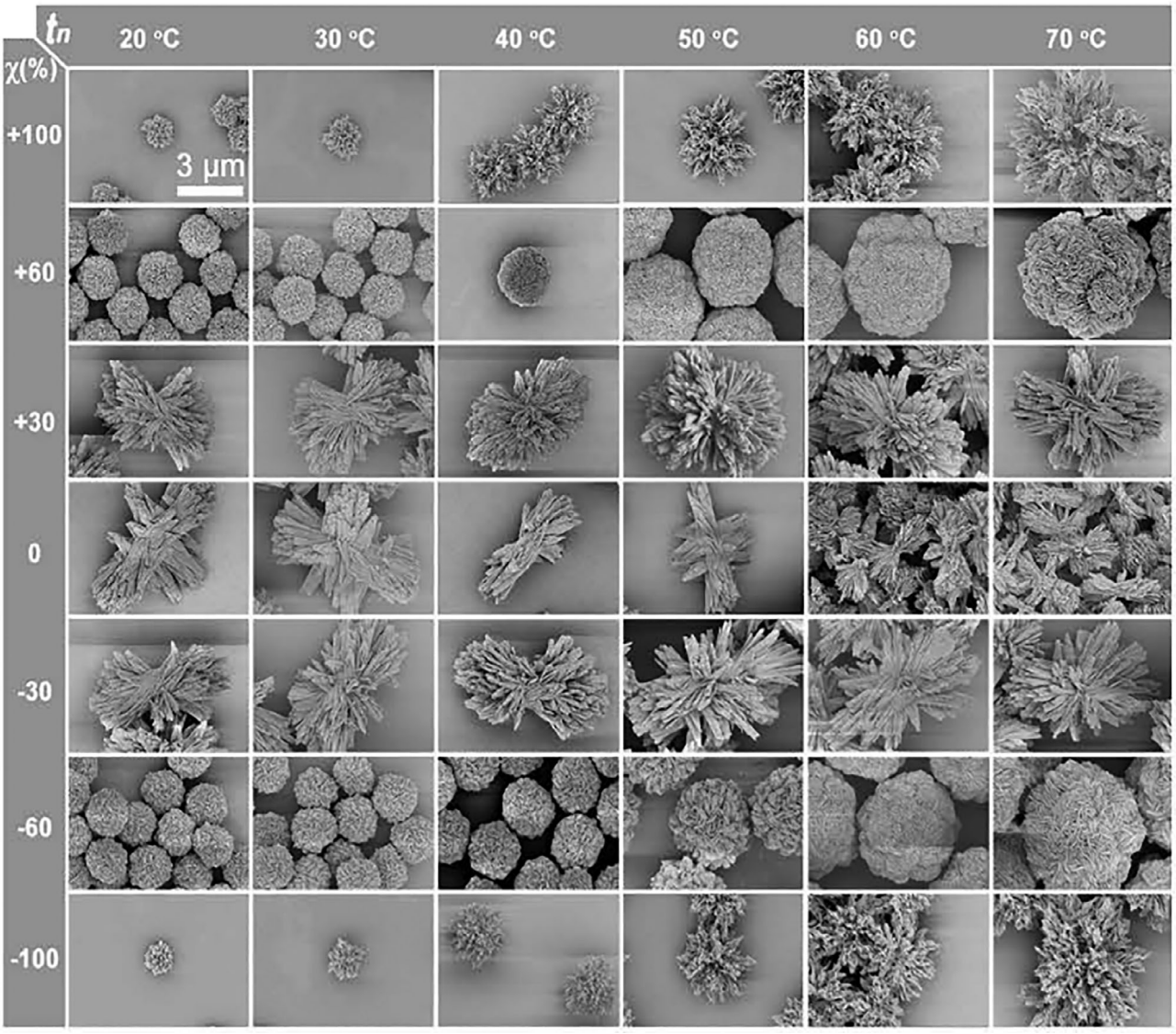

FIGURE 17 SEM images of Au-Cys supraparticles assembled at different values of nucleation temperatures (t_n) and enantiomeric excess (χ). Adapted with permission from Ref. 64 Copyright © 2020 The Authors, some rights reserved

Notably, the symmetric relations retained by all NPs in the dispersion, regardless of the polydispersity, are transferred into these multiparticle assemblies.[172] The importance of symmetric relations originates from the correlated motion between the NPs preceding the assembly, which is typical for the critical states and near-critical conditions in the system. Prior studies in thermodynamics, including the critical states in assemblies of surfactants, indicate that the symmetry of the system components plays a more important role than its polydispersity in determining the pathway for its evolution. Consequently, the polydispersity of the NPs does not inhibit, and may facilitate, the assembly of the superstructures. An example of such translation of chirality from NPs to their complex assemblies is the formation of the uniformly sized left- and right-handed helices from chiral CdTe NPs stabilized with *L*-Cys and *D*-Cys, respectively (Figure 14A).[67] CdTe NPs of tetrahedron shape assembled into enantiopure Boerdijk–Coxeter-Bernal helices as a result of the face-to-face attraction of the NPs that maximizes the number of coordination bridges and hydrogen bonds between them. The enantiomeric excess of these helices was 100% because the face-to-face contacts between NPs have angular displacement with respect to each other.

Also, *D*- and *L*-enantiomers of Asp and Glu AAs could induce the growth of chiral vaterite toroidal superstructures, which have a right-handed spiraling morphology induced by *L*-enantiomers of Asp and Glu, whereas left-handed morphology was induced by *D*-enantiomers (Figure 14B,C).[173] Such assembly pattern is related to NP tilting in the process of self-limited assembly.[173] This process occurs over various length scales and creates oriented inorganic platelets and chiral vaterite superstructures.

Another interesting type of system showing how chiral hierarchically organized architectures could arise from chiral molecules by non-classical pathway is optically active chiral supraparticles decorated

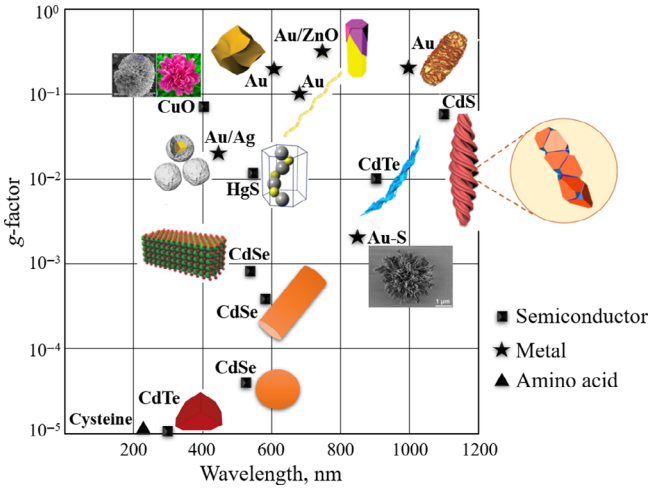

FIGURE 18 Maximum of the *g*-factor spectra reported for various chiral inorganic nanoparticles and their assemblies. The data are from Ref. 31, 58, 64, 67, 80, 103, 107, 116, 119, 175, 177, 183, 184

with spikes or sheets.[174–177] For example, right-handed twisting rod-like cellulose nanocrystals (CNCs) were used as a chiral template and building block for the formation of chiral CuO/CNC composite supraparticles (Figure 15A).[177] These CNCs had three levels of chirality: (i) molecular chirality of glucose units, (ii) structural chirality of the right-handed nanorods, and (iii) chirality of cholesteric liquid crystal structure. The supraparticles formed from helical nanopetals (Figure 15B) had a broadband chiroptical activity (Figure 15C) with anisotropy *g*-factors are small—0.002. After removing CNCs by calcination, the calcined CuO maintained the architecture and demonstrated intense chiroptical activity. As revealed later, these supraparticles could also be used for the engineering of materials with circularly polarized light emission. Note that some considerable number of studies refer to the circularly polarized light emitted from such nanostructured assemblies as circularly polarized luminescence. In many cases this is not quite accurate because the circular polarization on the nanostructured assemblies often originates from differential scattering. Besides significant difference in physics of the light-matter interactions, this distinction has direct relevance to engineering of these nanostructures for these properties.[174]

CuO NPs self-assemble into spiky supraparticles that are often referred to as flower-like particles, with diameters that range from 1.0 to 2.5 μm can also be prepared via a surfactant-mediated hydrothermal synthesis using sodium dodecyl sulfate as a structure-directing agent, amino alcohol as a symmetry-breaking agent, and cupric salt as the inorganic source.[175] In particular, CuO assemblies were synthesized with (S)-(−)- and (R)-(+)-2-amino-3-phenyl-1-propanol (S)-(−)- and (R)-(+)-APP) at 75 and 135 min, respectively (Figure 16A–D). Supraparticles from CuO assembled with many nanosheets stacked in a single direction and alternately connected, revealing the handedness of the helical structure. CuO assemblies formed with the (S)-(−)- and (*R*)-(+)-APP had the same structure but assembled in the opposite directions. Bands of diffused reflection circular dichroism (DRCD) spectra of these structures appeared to be in the CuO absorption region, confirming that the chiroptical activity of supraparticles originates from the chiral structure of the CuO (Figure 16E). The *g*-factors of CuO supraparticles do not exceed 0.08 (Figure 16F).

Hierarchically organized nanoarchitectures made in the presence of chiral molecules can be designed with complexity higher than in their biological counterparts.[64] Figure 17 demonstrates the diversity of hierarchically organized particles, which were formed under different temperature regimes with an enantiomeric excess of chiral molecules. Some of these structures are coccolith-like particles with *g*-factors ~0.005. The anisotropy factors for emitted photons were 0.0016 and 0.005 for Au/Cu-Cys and Au/Ag-Cys structures, respectively.

5 | CONCLUSIONS AND OUTLOOK

Chiral inorganic nanostructures have distinct fundamental importance but they are also essential for futher development of chemical, pharmaceutical, environmental, and biomedical technologies. Starting from the observation of exceptionally strong polarization rotation,[62] chiral nanostructures approach commercialization as biosensors due to favorable signal-to-noise ratio.[178] Shortly behind them in the commercialization que are their applications as catalysts,[39] polarization detectors,[179] and drug discovery platforms.[103,180] We also expect that chiral inorganic nanostructures will open new methods for chiral synthesis and separations for pharmaceutical industry due to steadily increasing importance and market percentage of chiral drugs.[181,182] Also, some other industries (e.g., polymers, insecticides) utilize chiral intermediates and chiral NP or their complex assemblies (Figure 17) can assist in their production, purification, storage, and utilization.

Chiral inorganic nanostructures can also be the products themselves, for instance due to their strong chiroptical or biological activity. Cumulative analysis of their chiroptical properties in Figure 18 indicates that the *g*-factors of these materials significantly surpass those of individual chiral organic molecules. Based on the clear trend of increased *g*-factor for longer wavelengths, chiral nanostructures provide particularly interesting prospects for the engineering of optical material in NIR and IR parts of the spectrum.[67] Even comparatively small metal NPs with 30 nm diameter can have *g*-factors ~0.02 at 450 nm.[183] The increase in size and complexity makes metal nanostructures to have *g*-factors up to 0.3 at 750 nm.[107] Semiconductor nanostructures also can be designed to have strong chiroptical activity, including 10–15 nm HgS NPs with *g*-factor ~0.012 at 750 nm[58] and self-assembled microscale long helices with *g*-factor ~0.06 at 1100.[67] Theoretical considerations also support the notion that *g*-factors of chiral semiconductor nanostructures can be increased up to 0.2 at ~124 μm by creating screw dislocations inside them.[105] This rich scientific background will allow to find new ways to compensate relatively low polarizabilities of some substances and get novel technologically advantageous materials.

The engineering tools discussed in this review can expand the field of chiral inorganic nanostructures within the next 10 years. The

strong chiroptical activity of chiral inorganic nanostructures and tunability of their CD and *g*-factor spectra will broaden the field of chiral photonics. While many of the mechanisms responsible for chiroptical activity can be described with some degree of clarity, there is still a lot of room for their improvement reaching, for instance *g*-factors approaching the theoretical maximum of 2. Note that most current displays and similar devices utilize chiroptical properties of liquid crystals produced from chiral molecules. Their long-range organization enhances their optical activity and asymmetries by multiple orders of magnitude compared to their molecular components. Recent data on inorganic chiral assemblies with liquid-crystal-like order indicate that the same effects can also be achieved for assemblies of chiral NPs.[103] In order to accomplish it, we need to understand and control the complex interplay of electrostatic, van der Waals, ionic interaction, and hydrogen bonding responsible for their formation better. A detailed account of the multiplicity of these interdependent interactions as a part of non-additivity theory[123] of nanoscale forces will constitute a large step forward both from fundamental and practical point of view.

Another research direction is the development of novel hierarchically organized nanostructures with reconfigurable chirality. Also, the discovery of chiral biases that ensure high enantiomeric excess, stability, and enhanced chiroptical activity is expected to be of importance. This can include studies on the formation of chiral structures using CPL, electric and magnetic fields.[31–33,155,157] Pathways to create chiral nanostructures with low polydispersity at large scale will make a step forward technological applicability of these materials.

The field of chiral nanostructures and their assemblies is actively growing, and there are many discoveries to be made. Among other promising directions that is starting to emerge, chiral inorganic nanostructures also represent a promising materials platform for enantioselective catalysis and various biomedical applications. In particular, the high efficacy and robustness of chiral inorganic nanostructures make them better catalysts than traditionally used materials. Also, chiral inorganic NPs can be designed as nanoscale agents with designed strong biological activity, for example, for regulation of immune system response. While many applications can be envisioned, all of them will require purposefully engineered chiral nanostructures at large scale, which is currently not yet present. We anticipate that it will be the most significant step in their future implementations. Development of methods of their self-assembly (Section 4.6) is expected to facilitate this process. Self-assembly in aqueous media make it more energy efficient and environmentally concision.

ACKNOWLEDGMENTS

Nicholas Kotov expresses deep gratitude to the American Institute of Chemical Engineers (AICHE) for the Alpha Chi Sigma Award. The review preparation process was primarily supported by Vannevar Bush DoD Fellowship to Nicholas Kotov titled "Engineered Chiral Ceramics" ONR N000141812876, NSF project "Energy- and Cost-Efficient Manufacturing Employing Nanoparticles" (NSF 1463474); NSF 1566460 "Nanospiked Particles for Photocatalysis"; NSF grant 1538180; NSF grant DMR-9871177 for funding the JEOL 2010F analytical electron microscope used in this work. Also partially supported by Office of Naval Research Multidisciplinary University Research Initiative Award ONR N00014-18-1-2497.

ORCID

Anastasia Visheratina https://orcid.org/0000-0001-7839-6496
Prashant Kumar https://orcid.org/0000-0003-4622-0917
Nicholas Kotov https://orcid.org/0000-0002-6864-5804

REFERENCES

1. Gallagher S, Moloney MP, Wojdyla M, Quinn SJ, Kelly JM, Gun'ko YK. Synthesis and spectroscopic studies of chiral CdSe quantum dots. *J Mater Chem*. 2010;20(38):8350. https://doi.org/10.1039/c0jm01185a
2. Xia Y, Zhou Y, Tang Z. Chiral inorganic nanoparticles: origin, optical properties and bioapplications. *Nanoscale*. 2011;3(4):1374-1382. https://doi.org/10.1039/c0nr00903b
3. Geison GL. *The Private Science of Louis Pasteur*. Princeton University Press; 2014.
4. Pasteur L. Sur Les Relations Qui Peuvent Exister Entre La Forme Crystalline, La Composition Chimique et Le Sens de La Polarization Rotatoire. *Ann Chim Phys*. 1848;24:442-459.
5. van't Hoff JH. Die Langerung Der Atome Im Raume. *Arch Neer*. 1874;9:445.
6. Le Bel JA. Sur Les Relations Qui Existent Entre Les Formules Atomiques Des Corps Organiques et Le Pouvoir Rotatoire de Leurs Solutions. *Bul Soc Chim Paris*. 1874;22:337-347.
7. Kelvin L. *Baltimore Lectures on Molecular Dynamics and the Wave Theory of Light*. C.J. Clay and Sons, Cambridge University Press Warehouse; 1904.
8. Rosanoff MA. On Fischer's classification of stereo-isomers. *J Am Chem Soc*. 1906;28(1):114-121.
9. Bijvoet JM, Peerdeman AF, Van Bommel AJ. Determination of the absolute configuration of optically active compounds by means of X-rays. *Nature*. 1951;168(4268):271-272.
10. Lutz M, Schreurs AMM. Was Bijvoet right? Sodium rubidium (+)-tartrate tetrahydrate revisited. *Acta Crystallogr Sect C Cryst Struct Commun*. 2008;64(8):m296-m299.
11. Cahn RS, Ingold CK, Prelog V. The specification of asymmetric configuration in organic chemistry. *Experientia*. 1956;12(3):81-94.
12. Lassaletta JM, Fernandez R. *Atropisomerism and Axial Chirality*. World Scientific; 2019.
13. Goldanskii VI, Kuz'min VV. Spontaneous mirror symmetry breaking in nature and the origin of life. Paper presented at: AIP Conference Proceedings; 1988; 180: 163-228.
14. Meurer KP, Vögtle F. Helical molecules in organic chemistry. *Org Chem*. 1985;1-76.
15. Yang M, Kotov NA. Nanoscale helices from inorganic materials. *J Mater Chem*. 2011;21(19):6775-6792.
16. Huang G, Mei Y. Helices in micro-world: materials, properties, and applications. *J Mater*. 2015;1(4):296-306.
17. Ma W, Xu L, De Moura AF, et al. Chiral inorganic nanostructures. *Chem Rev*. 2017;117(12):8041-8093. https://doi.org/10.1021/acs.chemrev.6b00755
18. Im SW, Ahn HY, Kim RM, et al. Chiral surface and geometry of metal nanocrystals. *Adv Mater*. 2019;1905758:1-20. https://doi.org/10.1002/adma.201905758
19. Qiu M, Zhang L, Tang Z, Jin W, Qiu C-W, Lei DY. 3D metaphotonic nanostructures with intrinsic chirality. *Adv Funct Mater*. 2018;28(45):1803147.
20. Wang Y, Xu J, Wang Y, Chen H. Emerging chirality in nanoscience. *Chem Soc Rev*. 2013;42(7):2930-2962. https://doi.org/10.1039/c2cs35332f

21. Kuznetsova V, Gromova Y, Martinez-Carmona M, et al. Ligand-induced chirality and optical activity in semiconductor nanocrystals: theory and applications. *Nanophotonics*. 2020;10(2):797-824.
22. Ni B, Cölfen H. Chirality communications between inorganic and organic compounds. *SmartMat*. 2021;2(1):17-32.
23. Xiao L, An T, Wang L, Xu X, Sun H. Novel properties and applications of chiral inorganic nanostructures. *Nano Today*. 2020;30:100824. https://doi.org/10.1016/j.nantod.2019.100824
24. Milton FP, Govan J, Mukhina MV, Gun'ko YK. The chiral nano-world: chiroptically active quantum nanostructures. *Nanoscale Horizons*. 2016;1(1):14-26. https://doi.org/10.1039/c5nh00072f
25. Kumar J, Thomas KG, Liz-Marzán LM. Nanoscale chirality in metal and semiconductor nanoparticles. *Chem Commun*. 2016;52(85):12555-12569. https://doi.org/10.1039/C6CC05613J
26. Hu Z, Meng D, Lin F, Zhu X, Fang Z, Wu X. Plasmonic circular dichroism of gold nanoparticle based nanostructures. *Adv Opt Mater*. 2019;7:1801590. https://doi.org/10.1002/adom.201801590
27. Cecconello A, Besteiro LV, Govorov AO, Willner I. Chiroplasmonic DNA-based nanostructures. *Nat Rev Mater*. 2017;2(9):17039. https://doi.org/10.1038/natrevmats.2017.39
28. Wen Y, He M-Q, Yu Y-L, Wang J-H. Biomolecule-mediated chiral nanostructures: a review of chiral mechanism and application. *Adv Colloid Interface Sci*. 2021;289:102376.
29. Luo Y, Chi C, Jiang M, et al. Plasmonic chiral nanostructures: chiroptical effects and applications. *Adv Opt Mater*. 2017;5(16):1700040.
30. Urban MJ, Shen C, Kong X-T, et al. Chiral plasmonic nanostructures enabled by bottom-up approaches. *Annu Rev Phys Chem*. 2019;70(1):275-299. https://doi.org/10.1146/annurev-physchem-050317-021332
31. Yeom J, Yeom B, Chan H, et al. Chiral templating of self-assembling nanostructures by circularly polarized light. *Nat Mater*. 2015;14(1):66-72. https://doi.org/10.1038/nmat4125
32. Kim J-Y, Yeom J, Zhao G, et al. Assembly of gold nanoparticles into chiral superstructures driven by circularly polarized light. *J Am Chem Soc*. 2019;141(30):11739-11744. https://doi.org/10.1021/jacs.9b00700
33. Saito K, Tatsuma T. Chiral plasmonic nanostructures fabricated by circularly polarized light. *Nano Lett*. 2018;18(5):3209-3212. https://doi.org/10.1021/acs.nanolett.8b00929
34. Safin F, Kolesova E, Maslov V, Gun'ko Y, Baranov A, Fedorov A. Photochemically induced circular dichroism of semiconductor quantum dots. *J Phys Chem C*. 2019;123(32):19979-19983.
35. Zhou Y, Yang M, Sun K, Tang Z, Kotov NA. Similar topological origin of chiral centers in organic and nanoscale inorganic structures: effect of stabilizer chirality on optical isomerism and growth of CdTe nanocrystals. *J Am Chem Soc*. 2010;132(17):6006-6013. https://doi.org/10.1021/ja906894r
36. Tohgha U, Deol KK, Porter AG, et al. Ligand induced circular dichroism and circularly polarized luminescence in CdSe quantum dots. *ACS Nano*. 2013;7(12):11094-11102. https://doi.org/10.1021/nn404832f
37. Liang Z, Bernardino K, Han J, et al. Optical anisotropy and sign reversal in layer-by-layer assembled films from chiral nanoparticles. *Faraday Discuss*. 2016;191:141-157. https://doi.org/10.1039/c6fd00064a
38. Suzuki N, Wang Y, Elvati P, et al. Chiral graphene quantum dots. *ACS Nano*. 2016;10(2):1744-1755. https://doi.org/10.1021/acsnano.5b06369
39. Li SS, Liu J, Ramesar NSNS, et al. Single- and multi-component chiral supraparticles as modular enantioselective catalysts. *Nat Commun*. 2019;10:4826. https://doi.org/10.1038/s41467-019-12134-4
40. Zhu Y, Guo J, Qiu X, Zhao S, Tang Z. Optical activity of chiral metal nanoclusters. *Acc Mater Res*. 2020;2:21-35.
41. Hazen RM, Sholl DS. Chiral selection on inorganic crystalline surfaces. *Nat Mater*. 2003;2(6):367-374. https://doi.org/10.1038/nmat879
42. Sholl DS, Gellman AJ. Developing chiral surfaces for enantioselective chemical processing. *AIChE J*. 2009;55(10):2484-2490.
43. Yeom J, Santos USS, Chekini M, Cha M, de Moura AF, Kotov NAA. Chiromagnetic nanoparticles and gels. *Science*. 2018;359(6373):309-314. https://doi.org/10.1126/science.aao7172
44. Jiang S, Chekini M, Qu ZB, et al. Chiral ceramic nanoparticles and peptide catalysis. *J Am Chem Soc*. 2017;139(39):13701-13712. https://doi.org/10.1021/jacs.7b01445
45. Elliott S, Moloney M, Gun'ko Y. Chiral shells and achiral cores in CdS quantum dots. *Nano Lett*. 2008;8(8):2452-2457.
46. Nakashima T, Kobayashi Y, Kawai T. Optical activity and chiral memory of thiol-capped CdTe nanocrystals. *J Am Chem Soc*. 2009;131(30):10342-10343. https://doi.org/10.1021/ja902800f
47. Jiang S, Chekini M, Qu Z, et al. Chiral ceramic nanoparticles of tungsten oxide and peptide catalysis. *J Am Chem Soc*. 2017;139:13701-13712. https://doi.org/10.1021/jacs.7b01445
48. Mukhina MV, Maslov VG, Baranov AV, et al. Intrinsic chirality of CdSe/ZnS quantum dots and quantum rods. *Nano Lett*. 2015;15(5):2844-2851. https://doi.org/10.1021/nl504439w
49. Sun M, Xu L, Qu A, et al. Site-selective photoinduced cleavage and profiling of DNA by chiral semiconductor nanoparticles. *Nat Chem*. 2018;10(8):821-830. https://doi.org/10.1038/s41557-018-0083-y
50. Meng F, Morin SA, Forticaux A, Jin S. Screw dislocation driven growth of nanomaterials. *Acc Chem Res*. 2013;46(7):1616-1626.
51. Wu H, Meng F, Li L, Jin S, Zheng G. Dislocation-driven CdS and CdSe nanowire growth. *ACS Nano*. 2012;6(5):4461-4468.
52. Adams LLA. Hexagonal spiral growth in the absence of a substrate. *Phys Rev E Stat Nonlin Soft Matter Phys*. 2010;82(3):31604.
53. Chen C-C, Zhu C, White ER, et al. Three-dimensional imaging of dislocations in a nanoparticle at atomic resolution. *Nature*. 2013;496(7443):74-77. https://doi.org/10.1038/nature12009
54. Bierman MJ, Lau YKA, Kvit AV, Schmitt AL, Jin S. Dislocation-driven nanowire growth and Eshelby twist. *Science*. 2008;320(5879):1060-1063.
55. Ben-Moshe A, da Silva A, Müller A, et al. The chain of chirality transfer in tellurium nanocrystals. *Science*. 2021;372(6543):729-733.
56. Boles MA, Talapin DV. Self-assembly of tetrahedral CdSe nanocrystals: effective "patchiness" via anisotropic steric interaction. *J Am Chem Soc*. 2014;136(16):5868-5871.
57. Yang YA, Wu H, Williams KR, Cao YC. Synthesis of CdSe and CdTe nanocrystals without precursor injection. *Angew Chem Int Ed*. 2005;44:6712-6715. https://doi.org/10.1002/anie.200502279
58. Wang P, Yu S-J, Govorov AO, Ouyang M. Cooperative expression of atomic chirality in inorganic nanostructures. *Nat Commun*. 2017;8:14312. https://doi.org/10.1038/ncomms14312
59. Lee HE, Ahn HY, Mun J, et al. Amino-acid- and peptide-directed synthesis of chiral plasmonic gold nanoparticles. *Nature*. 2018;556(7701):360-364. https://doi.org/10.1038/s41586-018-0034-1
60. Mastroianni AJ, Claridge SA, Paul Alivisatos A. Pyramidal and chiral groupings of gold nanocrystals assembled using DNA scaffolds. *J Am Chem Soc*. 2009;131(24):8455-8459. https://doi.org/10.1021/ja808570g
61. Fan Z, Govorov AO. Plasmonic circular dichroism of chiral metal nanoparticle assemblies. *Nano Lett*. 2010;10(7):2580-2587. https://doi.org/10.1021/nl101231b
62. Chen W, Bian A, Agarwal A, et al. Nanoparticle superstructures made by polymerase chain reaction: collective interactions of nanoparticles and a new principle for chiral materials. *Nano Lett*. 2009;9(5):2153-2159. https://doi.org/10.1021/nl900726s
63. Yan W, Xu L, Xu C, et al. Self-assembly of chiral nanoparticle pyramids with strong R/S optical activity. *J Am Chem Soc*. 2012;134(36):15114-15121. https://doi.org/10.1021/ja3066336

64. Jiang W, Qu Z, Kumar P, et al. Emergence of complexity in hierarchically organized chiral particles. *Science*. 2020;368(6491):642-648. https://doi.org/10.1126/science.aaz7949
65. Wang Y, Wang Q, Sun H, et al. Chiral transformation: from single nanowire to double helix. *J Am Chem Soc*. 2011;133(50):20060-20063.
66. Zhou Y, Ji Q, Masuda M, Kamiya S, Shimizu T. Helical arrays of CdS nanoparticles tracing on a functionalized chiral template of glycolipid nanotubes. *Chem Mater*. 2006;18(2):403-406.
67. Yan J, Feng W, Kim J-Y, et al. Self-assembly of chiral nanoparticles into semiconductor helices with tunable near-infrared optical activity. *Chem Mater*. 2020;32(1):476-488. https://doi.org/10.1021/acs.chemmater.9b04143
68. Singh G, Chan H, Baskin A, et al. Self-assembly of magnetite nanocubes into helical superstructures. *Science*. 2014;345(6201):1149-1153. https://doi.org/10.1126/science.1254132
69. Ma W, Kuang H, Wang L, et al. Chiral plasmonics of self-assembled nanorod dimers. *Sci Rep*. 2013;3:1934. https://doi.org/10.1038/srep01934
70. Zhang Q, Hernandez T, Smith KW, et al. Unraveling the origin of chirality from plasmonic nanoparticle-protein complexes. *Science*. 2019;365(6460):1475-1478. https://doi.org/10.1126/science.aax5415
71. Auguié B, Alonso-Gómez JL, Guerrero-Martínez A, Liz-Marzán LM. Fingers crossed: optical activity of a chiral dimer of plasmonic nanorods. *J Phys Chem Lett*. 2011;2(8):846-851. https://doi.org/10.1021/jz200279x
72. Lan X, Lu X, Shen C, Ke Y, Ni W, Wang Q. Au nanorod helical superstructures with designed chirality. *J Am Chem Soc*. 2015;137(1):457-462. https://doi.org/10.1021/ja511333q
73. Kuzyk A, Schreiber R, Zhang H, Govorov AO, Liedl T, Liu N. Reconfigurable 3D plasmonic metamolecules. *Nat Mater*. 2014;13(9):862-866. https://doi.org/10.1038/nmat4031
74. Qu A, Sun M, Kim J-Y, et al. Stimulation of neural stem cell differentiation by circularly polarized light transduced by chiral nanoassemblies. *Nat Biomed Eng*. 2020;5:103-113. https://doi.org/10.1038/s41551-020-00634-4
75. Osipov MA, Pickup BT, Dunmur DA. A new twist to molecular chirality: intrinsic chirality indices. *Mol Phys*. 1995;84:1193-1206. https://doi.org/10.1080/00268979500100831
76. Xu L, Ma W, Wang L, Xu C, Kuang H, Kotov NA. Nanoparticle assemblies: dimensional transformation of nanomaterials and scalability. *Chem Soc Rev*. 2013;42(7):3114-3126. https://doi.org/10.1039/c3cs35460a
77. Goodsell DS, Olson AJ. Structural symmetry and protein function. *Annu Rev Biophys Biomol Struct*. 2000;29:105-153.
78. Silva NHCS, Vilela C, Marrucho IM, Freire CSR, Neto CP, Silvestre AJD. Protein-based materials: from sources to innovative sustainable materials for biomedical applications. *J Mater Chem B*. 2014;2(24):3715-3740.
79. Makin OS, Serpell LC. Structures for amyloid fibrils. *FEBS J*. 2005;272(23):5950-5961.
80. Feng W, Kim J-Y, Wang X, et al. Assembly of mesoscale helices with near-unity enantiomeric excess and light-matter interactions for chiral semiconductors. *Sci Adv*. 2017;3(2):e1601159. https://doi.org/10.1126/sciadv.1601159
81. Hao C, Xu L, Kuang H, Xu C. Artificial chiral probes and bioapplications. *Adv Mater*. 2019;32:1802075. https://doi.org/10.1002/adma.201802075
82. Nakanishi K, Berova N, Woody RW. *Circular Dichroism: Principles and Applications*. Wiley-VCH; 2000.
83. Nafie LA. Infrared and Raman vibrational optical activity: theoretical and experimental aspects. *Annu Rev Phys Chem*. 1997;48(1):357-386.
84. Choi WJ, Cheng G, Huang Z, Zhang S, Norris TB, Kotov NA. Terahertz circular dichroism spectroscopy of biomaterials enabled by kirigami polarization modulators. *Nat Mater*. 2019;18(8):820-826. https://doi.org/10.1038/s41563-019-0404-6
85. Castiglioni E, Abbate S, Longhi G. Experimental methods for measuring optical rotatory dispersion: survey and outlook. *Chirality*. 2011;23(9):711-716.
86. Nafie LA. Vibrational optical activity: from discovery and development to future challenges. *Chirality*. 2020;32(5):667-692.
87. Barron LD, Hecht L, McColl IH, Blanch EW. Raman optical activity comes of age. *Mol Phys*. 2004;102(8):731-744.
88. Kurouski D. Advances of vibrational circular dichroism (VCD) in bioanalytical chemistry. A review. *Anal Chim Acta*. 2017;990:54-66.
89. Ranjbar B, Gill P. Circular dichroism techniques: biomolecular and nanostructural analyses – a review. *Chem Biol Drug Des*. 2009;74(2):101-120.
90. Kim Y, Yeom B, Arteaga O, et al. Reconfigurable chiroptical nanocomposites with chirality transfer from the macro- to the nanoscale. *Nat Mater*. 2016;15:461-468. https://doi.org/10.1038/NMAT4525
91. Arteaga O, Kahr B. Mueller matrix polarimetry of bianisotropic materials. *JOSA B*. 2019;36(8):F72-F83.
92. Houssier C, Sauer K. Circular dichroism and magnetic circular dichroism of the chlorophyll and protochlorophyll pigments. *J Am Chem Soc*. 1970;92(4):779-791.
93. Bosnich B. Application of exciton theory to the determination of the absolute configurations of inorganic complexes. *Acc Chem Res*. 1969;2(9):266-273.
94. Mason SF, Peart BJ. Crystal circular dichroism and spin-forbidden optical activity of tris-(diamine) cobalt (III) complexes. *J Chem Soc Dalton Trans*. 1977;(9):937-941.
95. Eaton WA, Charney E. Near-infrared absorption and circular dichroism spectra of ferrocytochrome c: D→ d transitions. *J Chem Phys*. 1969;51(10):4502-4505.
96. Moloney MP, Gun'ko YK, Kelly JM. Chiral highly luminescent CdS quantum dots. *Chem Commun*. 2007;7345(38):3900-3902. https://doi.org/10.1039/b704636g
97. Tohgha U, Varga K, Balaz M. Achiral CdSe quantum dots exhibit optical activity in the visible region upon post-synthetic ligand exchange with D- or L-cysteine. *Chem Commun (Camb)*. 2013;49(18):1844-1846. https://doi.org/10.1039/c3cc37987f
98. Kaschke J, Blume L, Wu L, et al. A helical metamaterial for broadband circular polarization conversion. *Adv Opt Mater*. 2015;3(10):1411-1417. https://doi.org/10.1002/adom.201500194
99. Visheratina A, Kotov NA. Inorganic nanostructures with strong Chiroptical activity. *CCS Chem*. 2020;2(3):583-604. https://doi.org/10.31635/ccschem.020.202000168
100. Gao X, Zhang X, Deng K, et al. Excitonic circular dichroism of chiral quantum rods. *J Am Chem Soc*. 2017;139(25):8734-8739. https://doi.org/10.1021/jacs.7b04224
101. Gao X, Zhang X, Zhao L, et al. Distinct excitonic circular dichroism between Wurtzite and Zincblende CdSe nanoplatelets. *Nano Lett*. 2018;18(11):6665-6671. https://doi.org/10.1021/acs.nanolett.8b01001
102. Rosenfeld L. Quantenmechanische Theorie Der Natürlichen Optischen Aktivität von Flüssigkeiten Und Gasen. *Zeitschrift für Phys*. 1928;52(3–4):161-174.
103. Lu J, Xue Y, Bernardino K, et al. Enhanced optical asymmetry in supramolecular chiroplasmonic assemblies with long-range order. *Science*. 2021;371(6536):1368-1374. https://doi.org/10.1126/science.abd8576
104. Baimuratov AS, Rukhlenko ID, Gun'ko YK, Baranov AV, Fedorov AV. Dislocation-induced chirality of semiconductor nanocrystals. *Nano Lett*. 2015;15(3):1710-1715. https://doi.org/10.1021/nl504369x

105. Baimuratov AS, Rukhlenko ID, Noskov RE, et al. Giant optical activity of quantum dots, rods, and disks with screw dislocations. *Sci Rep*. 2015;5:14712. https://doi.org/10.1038/srep14712
106. Kundelev EV, Orlova AO, Maslov VG, Baranov AV, Fedorov AV. Circular dichroism spectroscopy of complexes of semiconductor quantum dots with chlorin E6. *Nanophotonics VI – Int Soc Opt Photonics*. 2016;9884:988433.
107. Yeom B, Zhang H, Zhang H, et al. Chiral plasmonic nanostructures on achiral nanopillars. *Nano Lett*. 2013;13(11):5277-5283. https://doi.org/10.1021/nl402782d
108. Halasyamani PS, Poeppelmeier KR. Noncentrosymmetric oxides. *Chem Mater*. 1998;10(10):2753-2769.
109. Ben-Moshe A, Govorov AO, Markovich G. Enantioselective synthesis of intrinsically chiral mercury sulfide nanocrystals. *Angew Chemie Int Ed Engl*. 2013;52(4):1275-1279. https://doi.org/10.1002/anie.201207489
110. Zhou Y, Zhu Z, Huang W, et al. Optical coupling between chiral biomolecules and semiconductor nanoparticles: size-dependent circular dichroism absorption. *Angew Chem Int Ed Engl*. 2011;50(48):11456-11459. https://doi.org/10.1002/anie.201103762
111. Ben Moshe A, Szwarcman D, Markovich G. Size dependence of chiroptical activity in colloidal quantum dots. *ACS Nano*. 2011;5(11):9034-9043. https://doi.org/10.1021/nn203234b
112. Ben-Moshe A, Wolf SG, Sadan MB, et al. Enantioselective control of lattice and shape chirality in inorganic nanostructures using chiral biomolecules. *Nat Commun*. 2014;5:4302. https://doi.org/10.1038/ncomms5302
113. Sang Y, Han J, Zhao T, Duan P, Liu M. Circularly polarized luminescence in nanoassemblies: generation, amplification, and application. *Adv Mater*. 2019;1900110:1-33. https://doi.org/10.1002/adma.201900110
114. Lu X, Wu J, Zhu Q, et al. Circular dichroism from single plasmonic nanostructures with extrinsic chirality. *Nanoscale*. 2014;6(23):14244-14253. https://doi.org/10.1039/c4nr04433a
115. Losada M, Xu Y. Chirality transfer through hydrogen-bonding: experimental and Ab initio analyses of vibrational circular dichroism spectra of methyl lactate in water. *Phys Chem Chem Phys*. 2007;9(24):3127-3135.
116. Lee H, Kim RM, Ahn H, Rho J, Nam KT. Cysteine-encoded chirality evolution in plasmonic rhombic dodecahedral gold nanoparticles. *Nat Commun*. 2020;11(263):1-10. https://doi.org/10.1038/s41467-019-14117-x
117. Lee HE, Lee J, Ju M, et al. Identifying peptide sequences that can control the assembly of gold nanostructures. *Mol Syst Des Eng*. 2018;3(3):581-590. https://doi.org/10.1039/c7me00091j
118. Ji B, Panfil YE, Waiskopf N, Remennik S, Popov I, Banin U. Strain-controlled shell morphology on quantum rods. *Nat Commun*. 2019;10(1):1-9. https://doi.org/10.1038/s41467-018-07837-z
119. González-Rubio G, Mosquera J, Kumar V, et al. Micelle-directed chiral seeded growth on anisotropic gold nanocrystals. *Science*. 2020;368(6498):1472-1477. https://doi.org/10.1126/science.aba0980
120. De Yoreo JJ, Gilbert PUPA, Sommerdijk NAJMJM, et al. Crystallization by particle attachment in synthetic, biogenic, and geologic environments. *Science*. 2015;349(6247):aaa6760. https://doi.org/10.1126/science.aaa6760
121. Sau TK, Murphy CJ. Room temperature, high-yield synthesis of multiple shapes of gold nanoparticles in aqueous solution. *J Am Chem Soc*. 2004;126(28):8648-8649.
122. Kuo C-H, Huang MH. Synthesis of branched gold nanocrystals by a seeding growth approach. *Langmuir*. 2005;21(5):2012-2016.
123. Silvera Batista CA, Larson RG, Kotov NA. Nonadditivity of nanoparticle interactions. *Science*. 2015;350(6257):1242477 https://doi.org/10.1126/science.1242477
124. Guerrero-Martínez A, Alonso-Gómez JL, Auguié B, Cid MM, Liz-Marzán LM. From individual to collective chirality in metal nanoparticles. *Nano Today*. 2011;6(4):381-400. https://doi.org/10.1016/j.nantod.2011.06.003
125. Kuzyk A, Jungmann R, Acuna GP, Liu N. DNA origami route for nanophotonics. *ACS Photonics*. 2018;5(4):1151-1163. https://doi.org/10.1021/acsphotonics.7b01580
126. Shemer G, Krichevski O, Markovich G, Molotsky T, Lubitz I, Kotlyar AB. chirality of Silver nanoparticles synthesized on DNA. *J Am Chem Soc*. 2006;128(34):11006-11007. https://doi.org/10.1021/ja063702i
127. Chen C-L, Zhang P, Rosi NL. A new peptide-based method for the design and synthesis of nanoparticle superstructures: construction of highly ordered gold nanoparticle double helices. *J Am Chem Soc*. 2008;130(41):13555-13557. https://doi.org/10.1021/ja805683r
128. Kuzyk A, Schreiber R, Fan Z, et al. DNA-based self-assembly of chiral plasmonic nanostructures with tailored optical response. *Nature*. 2012;483(7389):311-314. https://doi.org/10.1038/nature10889
129. Wu X, Xu L, Liu L, et al. Unexpected chirality of nanoparticle dimers and ultrasensitive chiroplasmonic bioanalysis. *J Am Chem Soc*. 2013;135(49):18629-18636.
130. Lan X, Liu T, Wang Z, Govorov AO, Yan H, Liu Y. DNA-guided plasmonic helix with switchable chirality. *J Am Chem Soc*. 2018;140(37):11763-11770. https://doi.org/10.1021/jacs.8b06526
131. Nakano T, Okamoto Y. Synthetic helical polymers: conformation and function. *Chem Rev*. 2001;101(12):4013-4038. https://doi.org/10.1021/cr0000978
132. Ivanov VK, Fedorov PP, Baranchikov AY, Osiko VV. Oriented attachment of particles: 100 years of investigations of non-classical crystal growth. *Russ Chem Rev*. 2014;83(12):1204-1222. https://doi.org/10.1016/b978-0-08-012210-6.50078-8
133. Tang Z, Kotov NA, Giersig M. Spontaneous organization of single CdTe nanoparticles into luminescent nanowires. *Science*. 2002;297(5579):237-240.
134. Nakouzi E, Soltis JA, Legg BA, et al. Impact of solution chemistry and particle anisotropy on the collective dynamics of oriented aggregation. *ACS Nano*. 2018;12(10):10114-10122.
135. Zhang H, Banfield JF. Energy calculations predict nanoparticle attachment orientations and asymmetric crystal formation. *J Phys Chem Lett*. 2012;3(19):2882-2886.
136. Querejeta-Fernàndez A, Hernàndez-Garrido JC, Yang H, et al. Unknown aspects of self-assembly of PbS microscale superstructures. *ACS Nano*. 2012;6(5):3800-3812.
137. Yang M, Sun K, Kotov NA. Formation and assembly-disassembly processes of ZnO hexagonal pyramids driven by dipolar and excluded volume interactions. *J Am Chem Soc*. 2010;132(6):1860-1872. https://doi.org/10.1021/ja906868h
138. Zhu C, Liang S, Song E, et al. In-situ liquid cell transmission electron microscopy investigation on oriented attachment of gold nanoparticles. *Nat Commun*. 2018;9(1):1-7.
139. Yuk JM, Park J, Ercius P, et al. High-resolution EM of colloidal nanocrystal growth using graphene liquid cells. *Science*. 2012;336(6077):61-64. https://doi.org/10.1126/science.1217654
140. Li D, Nielsen MH, Lee JRI, Frandsen C, Banfield JF, De Yoreo JJ. Direction-specific interactions control crystal growth by oriented attachment. *Science*. 2012;336:1014-1018.
141. Penn RL, Banfield JF. Oriented attachment and growth, twinning, polytypism, and formation of metastable phases: insights from nanocrystalline TiO_2. *Am Mineral*. 1998;83(9–10):1077-1082.
142. Penn RL, Banfield JF. Imperfect oriented attachment: dislocation generation in defect-free nanocrystals. *Science*. 1998;281(5379):969-971. https://doi.org/10.1126/science.281.5379.969
143. Banfiel JF, Welch SA, Zhang H, Ebert TT, Penn RL. Aggregation-based crystal growth and microstructure development in natural

iron oxyhydroxide biomineralization products. *Science*. 2000; 289(5480):751-754. https://doi.org/10.1126/science.277.5327.788
144. Pacholski C, Kornowski A, Weller H. Self-assembly of ZnO: from nanodots to nanorods. *Angew Chem Int Ed Engl*. 2002;41(7): 1188-1191.
145. Lu W, Gao P, Jian WB, Wang ZL, Fang J. Perfect orientation ordered in-situ one-dimensional self-assembly of Mn-doped PbSe nanocrystals. *J Am Chem Soc*. 2004;126(45):14816-14821.
146. Zhang H, Huang F, Gilbert B, Banfield JF. Molecular dynamics simulations, thermodynamic analysis, and experimental study of phase stability of zinc sulfide nanoparticles. *J Phys Chem B*. 2003;107(47): 13051-13060.
147. Ondry JC, Hauwiller MR, Alivisatos P. Dynamics and removal pathway of edge dislocations in imperfectly attached PbTe nanocrystal pairs: toward design rules for oriented attachment. *ACS Nano*. 2018; 12(4):3178-3189. https://doi.org/10.1021/acsnano.8b00638
148. Tsai MH, Chen SY, Shen P. Imperfect oriented attachment: accretion and defect generation of nanosize rutile condensates. *Nano Lett*. 2004;4(7):1197-1201.
149. Liang H, Rossouw D, Zhao H, et al. Asymmetric silver " nanocarrot " structures: solution synthesis and their asymmetric plasmonic resonances. *J Am Chem Soc*. 2013;135(26):9616-9619. https://doi.org/10.1021/ja404345s
150. Reddy SS, Berchmans LJ, Sreedhar G. Imperfect oriented attachment of lanthanum hydroxide nanoparticles. *CrstEngComm*. 2019; 21(25):3829-3835.
151. Faccin GM, Pereira ZS, da Silva EZ. How crystallization affects the oriented attachment of silver nanocrystals. *J Phys Chem C*. 2021; 125(12):6812-6820.
152. Wang PP, Yu SJ, Ouyang M. Assembled suprastructures of inorganic chiral nanocrystals and hierarchical chirality. *J Am Chem Soc*. 2017; 139(17):6070-6073. https://doi.org/10.1021/jacs.7b02523
153. Srivastava S, Santos A, Critchley K, et al. Light-controlled self-assembly of semiconductor nanoparticles into twisted ribbons. *Science*. 2010; 327(5971):1355-1359. https://doi.org/10.1126/science.1177218
154. Feringa BL, van Delden RA. Absolute asymmetric synthesis: the origin, control, and amplification of chirality. *Angew Chem Int Ed Engl*. 1999;38(23):3418-3438. https://doi.org/10.1002/(SICI)1521-3773(19991203)38:23<3418::AID-ANIE3418>3.0.CO;2-V
155. Tran VT, Lee DK, Kim J, Jeong KJ, Kim CS, Lee J. Magnetic layer-by-layer assembly: from linear plasmonic polymers to oligomers. *ACS Appl Mater Interfaces*. 2020;12(14):16584-16591. https://doi.org/10.1021/acsami.9b22684
156. Jeong K-J, Lee DK, Tran VT, et al. Helical magnetic field-induced real-time plasmonic chirality modulation. *ACS Nano*. 2020;14(6): 7152-7160. https://doi.org/10.1021/acsnano.0c02026
157. Ma F, Wang S, Wu DT, Wu N. Electric-field-induced assembly and propulsion of chiral colloidal clusters. *Proc Natl Acad Sci U S A*. 2015; 112(20):6307-6312. https://doi.org/10.1073/pnas.1502141112
158. Decher G. Fuzzy nanoassemblies: toward layered polymeric multicomposites. *Science*. 1997;277(5330):1232-1237. https://doi.org/10.1126/science.277.5330.1232
159. Kotov NA. Ordered layered assemblies of nanoparticles. *MRS Bull*. 2001;26(12):992-997.
160. Lutkenhaus JL, Hammond PT. Electrochemically enabled polyelectrolyte multilayer devices: from fuel cells to sensors. *Soft Matter*. 2007;3(7):804-816. https://doi.org/10.1039/b701203a
161. Ariga K, Hill JP, Ji Q, et al. Layer-by-layer assembly as a versatile bottom-up nanofabrication technique for exploratory research and realistic application. *Phys Chem Chem Phys*. 2007;9(19):2319-2340. https://doi.org/10.1039/b700410a
162. Shiratori SS, Rubner MF. PH-dependent thickness behavior of sequentially adsorbed layers of weak polyelectrolytes. *Macromolecules*. 2000; 33(11):4213-4219.https://doi.org/10.1021/ma991645q
163. Kotov NA, Dékány I, Fendler JH. Ultrathin graphite oxide-polyelectrolyte composites prepared by self-assembly: transition between conductive and non-conductive states. *Adv Mater*. 1996; 8(8):637-641. https://doi.org/10.1002/adma.19960080806
164. Haddad A, Aharoni H, Sharon E, Shtukenberg AG, Kahr B, Efrati E. Twist renormalization in molecular crystals driven by geometric frustration. *Soft Matter*. 2019;15(1):116-126. https://doi.org/10.1039/C8SM01290C
165. Xia Y, Nguyen TDTD, Yang M, et al. Self-assembly of self-limiting monodisperse supraparticles from polydisperse nanoparticles. *Nat Nanotechnol*. 2011;6(9):580-587. https://doi.org/10.1038/nnano.2011.121
166. Park J, Nguyen TD, de Queirós Silveira G, et al. Terminal supraparticle assemblies from similarly charged protein molecules and nanoparticles. *Nat Commun*. 2014;5:3593. https://doi.org/10.1038/ncomms4593
167. Yang Y, Meyer RB, Hagan MF. Self-limited self-assembly of chiral filaments. *Phys Rev Lett*. 2010;104(25):258102. https://doi.org/10.1103/PhysRevLett.104.258102
168. Lenz M, Witten TA. Geometrical frustration yields fibre formation in self-assembly. *Nat Phys*. 2017;13(11):1100-1104. https://doi.org/10.1038/nphys4184
169. Grason G, Perspective M. Geometrically frustrated assemblies. *J Chem Phys*.2016;145(11):110901.https://doi.org/10.1063/1.4962629
170. de Queirós Silveira G, Ramesar N, Nguyen T, Bahng J, Glotzer S, Kotov N. Supraparticle nanoassemblies with enzymes. *Chem Mater*. 2019;31(18):7493-7500. https://doi.org/10.1021/acs.chemmater.9b02216
171. Yousefi AM, Zhou Y, Querejeta-Fernández A, Sun K, Kotov NA. Streptavidin inhibits self-assembly of CdTe nanoparticles. *J Phys Chem Lett*.2012;3(22):3249-3256.https://doi.org/10.1021/jz301455b
172. Qu Z, Feng W-J, Wang Y, Romanenko F, Kotov NA. Diverse nanoassemblies of graphene quantum dots and their mineralogical counterparts. *Angew Chem*. 2020;59(22):8542-8551. https://doi.org/10.1016/0009-2509(62)87032-8
173. Jiang W, Pacella MS, Athanasiadou D, et al. Chiral acidic amino acids induce chiral hierarchical structure in calcium carbonate. *Nat Commun*. 2017;8:15066. https://doi.org/10.1038/ncomms15066
174. Zhao B, Yu H, Pan K, Tan Z, Deng J. Multifarious chiral nanoarchitectures serving as handed-selective fluorescence filters for generating full-color circularly polarized luminescence. *ACS Nano*. 2020;14(3):3208-3218. https://doi.org/10.1021/acsnano.9b08618
175. Duan Y, Liu X, Han L, et al. Optically active chiral CuO "nanoflowers". *J Am Chem Soc*. 2014;136(20):7193-7196. https://doi.org/10.1021/ja500197e
176. Qian Y, Duan Y, Che S. Chiral nanostructured CuO films with multiple optical activities. *Adv Opt Mater*. 2017;5:1601013. https://doi.org/10.1002/adom.201601013
177. Yu H, Huang H, Liang J, Deng J. Twisted bio-nanorods serve as a template for constructing chiroptically active nanoflowers. *Nanoscale*. 2018; 10(25):12163-12168.https://doi.org/10.1039/C8NR03124J
178. Zhao Y, Xu L, Ma W, et al. Shell-engineered chiroplasmonic assemblies of nanoparticles for zeptomolar DNA detection. *Nano Lett*. 2014;14(7):3908-3913. https://doi.org/10.1021/nl501166m
179. Long G, Sabatini R, Saidaminov MI, et al. Chiral-perovskite optoelectronics. *Nat Rev Mater*. 2020;5:423-443. https://doi.org/10.1038/s41578-020-0181-5
180. Kumar J, Eraña H, López-Martínez E, et al. Detection of amyloid fibrils in Parkinson's disease using plasmonic chirality. *Proc Natl Acad Sci*. 2018;115(13):3225-3230. https://doi.org/10.1073/pnas.1721690115
181. Rouhi A. Chiral business: fine chemicals companies are jockeying for position to deliver the increasingly complicated chiral small molecules of the future. *Chem Eng News*. 2003;81(18):56-61.

182. Challener CA. Expanding the chiral toolbox. *Pharm Technol*. 2016; 40(7):28-29.
183. Wu X, Xu L, Ma W, et al. Gold core-DNA-silver shell nanoparticles with intense plasmonic chiroptical activities. *Adv Funct Mater*. 2015; 25(6):850-854. https://doi.org/10.1002/adfm.201403161
184. Yang G, Kazes M, Oron D. Chiral 2D colloidal semiconductor quantum wells. *Adv Funct Mater*. 2018;1802012. https://doi.org/10.1002/adfm.201802012

How to cite this article: Visheratina A, Kumar P, Kotov N. Engineering of inorganic nanostructures with hierarchy of chiral geometries at multiple scales. *AIChE J*. 2022;68(1): e17438. doi:10.1002/aic.17438